Lab on a Chip

PAPER

View Article Online
View Journal | View Issue

Check for updates

Cite this: *Lab Chip*, 2025, **25**, 155

A 3D-printed multi-compartment organ-on-chip platform with a tubing-free pump models communication with the lymph node†

Sophie R. Cook,[a] Alexander G. Ball,[bc] Anwaruddin Mohammad[d] and Rebecca R. Pompano *[ace]

Received 3rd June 2024,
Accepted 28th November 2024

DOI: 10.1039/d4lc00489b

rsc.li/loc

Multi-organ-on-chip systems (MOOCs) have the potential to mimic communication between organ systems and reveal mechanisms of health and disease. However, many existing MOOCs are challenging for non-experts to implement due to complex tubing, electronics, or pump mechanisms. In addition, few MOOCs have incorporated immune organs such as the lymph node (LN), limiting their applicability to model critical events such as vaccination. Here we developed a 3D-printed, user-friendly device and companion tubing-free impeller pump with the capacity to co-culture two or more tissue samples, including a LN, under a recirculating common media. Native tissue structure and immune function were incorporated by maintaining slices of murine LN tissue *ex vivo* in 3D-printed mesh supports for at least 24 h. In a two-compartment model of a LN and an upstream injection site in mock tissue, vaccination of the multi-compartment chip was similar to *in vivo* vaccination in terms of locations of antigen accumulation and acute changes in activation markers and gene expression in the LN. We anticipate that in the future, this flexible platform will enable models of multi-organ immune responses throughout the body.

Introduction

Molecular communication between organs is essential for life, both to maintain homeostasis and to respond rapidly to perturbation.[1] A key example is vaccination, which requires proper drainage of signals from the site of injection to the draining lymph node (LN) to initiate early inflammatory activation and, ultimately, protective immunity. However, it is challenging to isolate the communication between specific organs using *in vivo* models because many organs contribute simultaneously through blood and lymphatic vasculature. Multi-organ-on-chip (MOOC) technology addresses this challenge by connecting compartmentalized models of select organs together under well-controlled conditions, often with circulating blood or lymph-like media.[2–38] To provide well-controlled mass transport between compartments and reproducible flow and shear rates, MOOCs must have precise and controllable flow speeds, including with thick 3D cultures. MOOCs with recirculating fluid flow provide biological feedback loops between organs, allowing accumulation of otherwise dilute secreted factors and minimal media consumption.[26] However, despite their potential, MOOCs have not yet seen broad adoption by biomedical researchers.

For users focused on applications rather than microfluidics, the ease of use, compatibility with off-chip analysis, scalability for well-powered hypothesis testing, and reproducible and affordable fabrication are all just as critical as biomimicry.[5,8] These requirements are currently unmet for three reasons. First, most approaches for precisely controlled recirculating flow through MOOCs require extensive tubing and sophisticated electrical or pneumatic control systems, making them challenging for non-experts to implement.[39] Two solutions currently in development are the rotary planar peristaltic micropump and the 3D-printed centrifugal pump, both small integrated pumps that drive fluid flow on-chip without the need for tubing.[40,41] Closed-box commercial systems are also beginning to be available and are designed to be easy to use, but at a high cost. Second, many OOCs house the cell or tissue culture permanently inside of a sealed device, such as on a membrane inside of a microchannel, making it difficult to add tissues on demand or to remove them for imaging, flow cytometry, or gene expression analysis during or after the experiment.[8] Third,

[a] *Department of Chemistry, University of Virginia, Charlottesville, VA, USA. E-mail: rpompano@virginia.edu*
[b] *Department of Microbiology, Immunology, and Cancer Biology, University of Virginia, Charlottesville, VA, USA*
[c] *Carter Immunology Center and UVA Comprehensive Cancer Center, University of Virginia, Charlottesville, VA, USA*
[d] *Bioinformatics Core, University of Virginia, Charlottesville, VA, USA*
[e] *Department of Biomedical Engineering, University of Virginia, Charlottesville, VA, USA*

† Electronic supplementary information (ESI) available: The ESI data file includes all supplemental figures, supplemental tables, and the caption for Movie S1. See DOI: https://doi.org/10.1039/d4lc00489b

Open Access Article. Published on 02 December 2024. Downloaded on 5/13/2026 2:24:47 PM. This article is licensed under a Creative Commons Attribution-NonCommercial 3.0 Unported Licence.

Open Access Article. Published on 02 December 2024. Downloaded on 5/13/2026 2:24:47 PM.
This article is licensed under a Creative Commons Attribution-NonCommercial 3.0 Unported Licence.

although many OOCs are hand-assembled in polydimethylsiloxane (PDMS), broad adoption for statistically powered biological experiments requires more reproducible fabrication methods, such as 3D printing, machining, or embossing.[42,43] While there have been major advancements in MOOC technology, there is still a need for an easy-to-use multi-tissue chip that incorporates well-controlled fluid flow past biomimetic and experimentally accessible 3D cultures.

In addition to user-friendly technology, incorporation of organs of the immune system into MOOCs is an exciting frontier and is particularly dependent on inter-organ fluid flow. So far, MOOCs have primarily incorporated tissue-resident immune cells or recirculating white blood cells into existing models of lung, gut, brain, tumor, islets, *etc.*[4,44–47] Incorporation of models of dedicated immune organs such as the lymph node (LN) is a major next step to model systemic immune responses such as vaccination, infection, and autoimmunity.[48,49] LNs are small organs located along lymphatic vessels, where they filter flowing lymph fluid to detect and respond to pathogens (Fig. 1a).[50] Vaccination takes advantage of this system by inducing the adaptive immune response to protect against infection, with initial responses occurring within hours due to fluidic transport from the injection site.[51] Microscale and organoid models of the LN are still in early stages even in isolation,[48,52–61] let alone in connection with other organs.[27,62,63] The model with the longest history is *ex vivo* LN slice culture, which has been used to model the response to infection and vaccination in humans and animals for thirty years.[64–68]

Here, we developed a user-friendly, self-contained multi-compartment platform capable of multi-tissue co-culture under continuous recirculating fluid flow, and applied it to model the

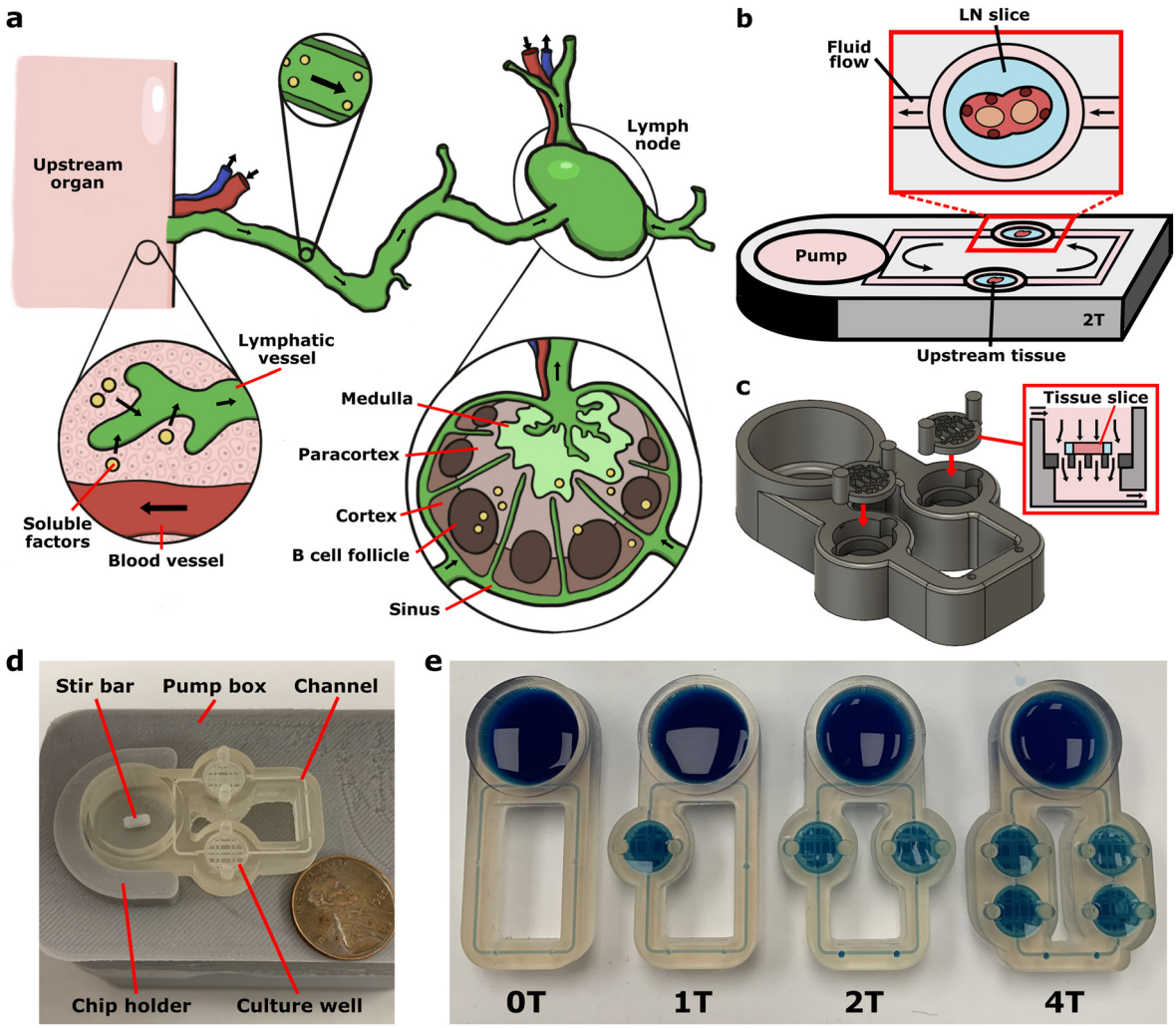

Fig. 1 Modeling communication with the lymph node using a multi-compartment chip. (a) Illustration of communication *via* soluble factors (*yellow dots*) from an upstream organ to local lymph nodes *via* lymphatic vessels and interstitial fluid flow through each organ. (b) Schematic of the multi-compartment device, which consisted of a loop of channels containing wells for tissue slice culture connected to a pump well. (c) 3D rendering of the device showing the insertion of the removable mesh support into the open top of the culture well. The mesh support holds a tissue slice suspended within the well to enable flow perpendicular to the tissue. (d) Photo of a two-compartment device (ITX-PEGDA resin) mounted on the motor-based impeller pump external platform, with a US penny for scale. (e) Photo of four variations of the device (ITX-PEGDA resin) containing zero (0T), one (1T), two (2T), and four (4T) wells for tissue slice culture. Each chip was filled with blue food dye to visualize the channels.

 This journal is © The Royal Society of Chemistry 2025

Open Access Article. Published on 02 December 2024. Downloaded on 5/13/2026 2:24:47 PM. This article is licensed under a Creative Commons Attribution-NonCommercial 3.0 Unported Licence.

communication between the lymph node and upstream drainage sites. Inspired by prior work integrating pumps directly into a device to minimize tubing,[26,69–74] and particularly by the simplicity of on-chip magnetic impeller pumps,[22,75,76] we developed a 3D-printed multi-compartment device and companion tubing-free motor-based impeller pump. The system was designed to be customizable for the needs of the user, including to change the number of tissue compartments and volumes. As a proof-of-concept, we used this platform to develop a model of the acute response to vaccination in murine LN slices, and tested its fidelity against *in vivo* vaccination in terms of antigen drainage and processing, early markers of activation, and changes in gene expression.

Experimental

Device fabrication and assembly

The microfluidic devices and removable mesh supports were designed using Fusion 360. Designs for the devices and removable mesh insert were deposited in a public repository (see Data availability below). Devices were printed in MiiCraft Clear resin (CADworks3D, Toronto, Canada) and in a custom PEGDA resin (ITX-PEGDA resin) formulated from a previously developed recipe.[77] The PEGDA resin consisted of poly(ethylene glycol) diacrylate (PEGDA, 250 MW, Sigma Aldrich) as the monomer, phenylbis(2,4,6-trimethylbenzoyl) phosphine oxide (Irgacure 819, Sigma Aldrich) as the photoinitiator, and isopropylthioxanthone (ITX, Fisher Scientific, New Hampshire, USA) as the photoabsorber. Irgacure 819 and ITX were mixed with PEGDA (0.4% w/w) using a vortex mixer and dissolved for 30 min at 70 °C.

Devices and mesh supports were printed using a CADWorks3D MiiCraft P110Y DLP printer (CADWorks3D, Toronto, Canada). All layers were printed at 50 μm at 100% power (5 mW cm^{-2}), 1.25 s cure time, 4 s base cure time, 6 base layers, and 4 buffer layers. For post-processing, all printed parts were submerged in isopropyl alcohol (IPA) in a Form Wash (FormLabs, Massachusetts, USA) for 4 min, dried thoroughly with nitrogen, and placed in a Form Cure high-intensity UV light box (10 mW cm^{-2}, FormLabs, Massachusetts, USA) for 1 min at room temperature. For device post-processing, channels were flushed with IPA using a wash bottle to clear channels of uncured resin before cleaning the chip in the Form Wash.

Preparation of 3D-printed material for tissue culture

To improve biocompatibility of the 3D-printed material, the device and mesh supports were coated in Parylene C as described previously.[78] In brief, a film of ~1 μm was achieved by adding 1.1 g of mixed isomers of Parylene C (SCS, Inc., Indianapolis, IN, USA) to the Labcoater 2 parylene coater (SCS, Inc., Indianapolis, IN, USA) for gas-phase deposition onto the prints. Prior to culture of tissue in any 3D-printed device, the print and stir bar were sterilized by submerging in 70% ethanol for 5 min, followed by two 10 min rinses in 1xPBS (Lonza, Maryland, USA). Once rinsed, the materials were allowed to air dry for at least 30 min before use. The removable mesh supports were loaded into the devices as needed and filled with complete media to the specified volume per device. The chips were then loaded onto the external pump platforms, which were turned on and placed in the incubator for at least 30 min before use to reach 37 °C.

Motor-based impeller pump assembly

The 3D-printed external housing, chip holder, and chip cover were designed using Fusion 360 and printed using 1.75 mm polylactic acid (PLA) filament (Flashforge, China) using a Monoprice Voxel 3D printer (Monoprice, California, USA). Designs for all of the pump-related files were deposited in a public repository (see Data Availability below). To assemble the motor-based impeller pump, a 6–12 V Mini DC motor (AUTOTOOLHOME) was inserted into the base of the printed housing. A custom magnet holder containing a small fan was 3D printed using the DLP printer described above in the ITX-PEGDA resin. The fan was included on the magnet mount to help push air down through the vents on the top of the motor and mitigate any heat buildup. Two 6 mm brushed nickel magnets (FINDMAG) with a strength of 0.008 T were glued using superglue into the magnet holder and mounted on the rotating pin of the DC motor.[75] Each motor was connected to a mini digital DC voltmeter (2.5–30 V, MakerFocus, China) and a pulse-width modulation (PWM) low voltage DC potentiometer (ALDECO), both mounted to their respective holes within the housing base. Within each pump, three anodized aluminum heatsinks (1 g, Easycargo) were mounted along the sides to help distribute heat away from the DC motor. Once assembled, the housing top was initially glued together with hot glue, and the seam was sealed with an epoxy to generate a moisture-free environment within the box. The chip holder was glued to the top of the external housing centered over the DC motor. Each pump was connected to a 12 V DC female power connector (Chanzon), which was plugged into the 12 V AC DC power supply adapter wall plug (EWETON). A cord splitter was used to connect all 8 pumps to a single power supply. All wiring was connected using a tin–lead rosin-core solder wire (ICESPRING) and wrapped in heat shrink tubing (Eventronic, Germany).

A Teflon PTFE encapsulated magnetic stir bar, either 2 × 5 mm (VWR, Pennsylvania, USA) or 3 × 10 mm (Thomas Scientific, New Jersey, USA) were used as impellers. The 2 × 5 mm stir bar was used for all experiments unless noted otherwise. A digital laser photo tachometer (AGPtek, New York, USA) was used to measure the revolutions per minute (RPM) of the magnetic stir bar as it rotated. All RPMs reported were conducted for each individual pump for corresponding voltages, and are the average of three RPM measurements made at a consistent voltage. Stir bar stability and pump heat emission were measured as reported previously.[75]

Characterization of experimental velocity within the device

The maximum velocity was measured experimentally as described previously.[75] In brief, a drop of blue food coloring

Open Access Article. Published on 02 December 2024. Downloaded on 5/13/2026 2:24:47 PM. This article is licensed under a Creative Commons Attribution-NonCommercial 3.0 Unported Licence.

was pipetted into a port within the device and tracked using a Dino-Lite Edge 3.0 digital microscope (SunriseDino, California, USA). For each velocity measurement, we allowed for 1–2 min of equilibration after either changing the pump voltage or flushing the channels with a pipette. Images were collected over time with a timestamp to the millisecond decimal place, and the distance the dye moved over time was measured to determine fluid velocity.

Animal model

All animal work was approved by the Institutional Animal Care and Use Committee at the University of Virginia under protocol #4042, and was conducted in compliance with guidelines from the University of Virginia Animal Care and Use Committee and the Office of Laboratory Animal Welfare at the National Institutes of Health (United States). Inguinal, axial, and brachial lymph nodes were harvested from female and male C57BL/6 mice (Jackson Laboratory, USA) under the age of 6 months following humane isoflurane anesthesia and cervical dislocation. There were no noticeable differences in viability (n = 2 M and 2 F), vaccine activation marker expression (n = 2 M and 1 F), or gene expression (n = 6 M and 6 F) between sexes, although these experiments were not powered to detect such differences. The lymph nodes were collected into "complete RPMI" media consisting of RPMI (Lonza, Maryland, USA) supplemented with 10% FBS (Corning, New York, USA), 1 × L-glutamine (Gibco Life Technologies, Maryland, USA), 50 U mL^{-1} Pen/Strep (Gibco Life Technologies, Maryland, USA), 50 μM beta-mercaptoethanol (Gibco Life Technologies, Maryland, USA), 1 mM sodium pyruvate (Hyclone, Utah, USA), 1× non-essential amino acids (Hyclone, Utah, USA), and 20 mM HEPES (VWR, Pennsylvania, USA).

Preparation of lymph node slices

To generate lymph node slices, the inguinal, axial, and brachial lymph nodes were inserted into 6% w/v low melting point agarose (Lonza, Maryland, USA) in 1xPBS and punched into 5 mm blocks using a disposable biopsy punch (Royaltek).[68] The 300 μm slices were generated using a Leica VT1000S vibratome (Illinois, USA) set to a speed of 90 (0.17 mm s^{-1}) and a frequency of 3 (30 Hz) while submerged in ice cold PBS. Slices were collected and placed in a 6-well plate containing ~3 mL per well of complete media and placed in a sterile cell culture incubator (37 °C with 5% CO_2) for 1 h to rest prior to use.

Measurement of viability of primary murine LN tissue

For resin cytotoxicity measurements, simple wells similar in size to the pump well were 3D printed and parylene coated as described above. The printed wells were inserted into a 12 well plate and filled with 1000 μL of fresh media, with empty well plate wells used as a plate control. The plate was equilibrated in the cell culture incubator at 37 °C for at least 30 min, after which LN slices from different nodes were randomly added to each well and cultured for 24 h.

For on-chip culture, the chips, mesh inserts, and stir bars were sterilized and dried as described above. Once dry, the mesh support(s) and stir bar were loaded into each device before filling with 1600 μL of fresh media. The channels were flushed through the ports using a pipette to ensure there were no bubbles hindering fluid flow. Chips were loaded onto the pump platforms and covered with a FDM 3D-printed cover, and the pumps were set to the required speed. The whole chip and pump assembly was equilibrated in the cell culture incubator for at least 30 min before tissue slices were added, after which slices from different nodes were randomly added to the culture wells containing mesh supports and cultured for 24 h. All cell and tissue viability experiments consisted of two identical experiments performed on different days pooled together to test reproducibility.

Following the culture period, LN slice viability was assessed using a CellTiter 96® AQ_{ueous} One Solution Cell Proliferation Assay (MTS assay, Promega, Wisconsin, USA). Intact slices were added directly to 100 μL of media in a 96 well plate. A killed control was generated by adding 15 μL of 10× Lysis Buffer (CyQUANT LDH Cytotoxicity Assay Kit, Invitrogen, Massachusetts, USA) to the media for 30 min at 37 °C. Next, 50 μL of fresh media was added to each well. Then, 30 μL of CellTiter One Solution Reagent was added to each well and incubated for 3 h at 37 °C. At the end of the culture period, 100 μL of media was transferred to fresh wells on the same plate. Bubbles were removed by centrifugation for 5 min at 400 × g. Absorbance was measured at 490 nm using a CLARIOstar plate reader (BMG LabTech, Germany). The background absorbance from media-only controls were subtracted from the live and killed controls and samples.

Soluble factor recirculation and capture on-chip

To generate mock tissue, biotinylated magnetic beads (0.5 μm beads, RayBiotech, Georgia, USA) were embedded in 3% w/v agarose (Lonza, Maryland, USA) in 1× PBS (Lonza, Maryland, USA), which was cast in a 3 mm punched hole within a 35 mm petri dish filled with solidified 6% w/v agarose. This was punched into 5 mm blocks with the bead-laden gel in the center using a disposable biopsy punch (Royaltek). Blocks were sliced to a thickness of 300 μm as described above using previously reported methods.[68] Slices were collected and placed in a 6-well plate containing 1× PBS. Prior to protein insertion, the channels of the device (ITX-PEGDA resin) were blocked with BSA (bovine serum albumin) by filling the device 1% BSA (Fisher Scientific, New Hampshire, USA) in 1× PBS (Lonza, Maryland, USA) and recirculating at 1250 RPM (1.7 V, 75 μm s^{-1} maximum channel velocity) for 1 h. A biotin bead-loaded slice was added to a culture well within the device, and 5 μL of 200 μg mL^{-1} NeutrAvidin™ Rhodamine Red™-X (NRho, Fisher Scientific, New Hampshire, USA) was pipetted to the opposite culture well upstream of the slice. The biotin-bead loaded

 This journal is © The Royal Society of Chemistry 2025

Open Access Article. Published on 02 December 2024. Downloaded on 5/13/2026 2:24:47 PM.
This article is licensed under a Creative Commons Attribution-NonCommercial 3.0 Unported Licence.

slices were removed from the device using the removable mesh insert and imaged at 0 h (before NRho addition), 0.5 h, 1 h, 2 h, 4.3 h, and 24.6 h using a Zeiss Axio Zoom macroscope (Carl Zeiss Microscopy, Germany). All images were analyzed in ImageJ, where the background-subtracted mean gray value of the entire tissue slice was calculated.[79]

DQ-OVA capture in live LN slices on-chip

LNs were sliced as described above. To generate a killed control for on-chip and off-chip culture, during the 1 h rest period after tissue slicing, a portion of the slices were transferred to a 24 well plate containing 2 mL of 35% ethanol for 30 min, then moved to a new well containing 1× PBS for a 30 min rinse. Live and killed slices were cultured both on-chip and off-chip in the presence of DQ-ovalbumin (DQ-OVA, Invitrogen, Massachusetts, UVA). Following the 1 h rest per kill periods, the slices were added to either a well plate or the downstream tissue culture well of a 2T chip, both filled with 1800 μL of complete media. For the on-chip conditions, 10 μL of 500 μg mL^{-1} DQ-OVA was added to the upstream culture well. Similarly, 10 μL of 500 μg mL^{-1} DQ-OVA was added directly to each off-chip culture well of the well plate. The slices were imaged at 0 h (before DQ-OVA addition), 2 h, 4 h, and 24 h on the Zeiss Axio Zoom macroscope. The off-chip slices were imaged within the well plate, while the on-chip slices were removed on the mesh supports and placed on a sterile petri dish for imaging before re-insertion. The slices were analyzed using ImageJ, where the background-subtracted mean gray value of the entire tissue slice was calculated. All images were leveled the same unless stated otherwise. The data presented consisted of two identical experiments performed on different days to demonstrate reproducibility.

Comparative vaccination on-chip, *in vivo*, and well plate

For *in vivo* vaccinations, male and female C57Bl/6 mice were vaccinated subcutaneously with four 50 μL injections per animal at the shoulders and hips. The vaccine consisted of 100 μg mL^{-1} R848 (InvivoGen) and 500 μg mL^{-1} rhodamine-labeled ovalbumin (Rho-OVA) in sterile 1× PBS, or PBS as a vehicle control. The skin-draining lymph nodes (axillary, brachial, and inguinal) were harvested either 24 h later for the imaging experiment or 6 h later for the RNA sequencing experiment.

For on-chip and well plate (wells) conditions, "mock skin" blocks were generated by punching 5 mm cylinders out of 6% agarose gel with a biopsy punch. The cylinders were placed on parafilm in a petri dish and excess liquid was gently removed. The vaccine solution, either 0.2 μg mL^{-1} R848 and 2 μg mL^{-1} Rho-OVA or PBS, was pipetted directly on top of each gel block and allowed to passively diffuse into the gel for 30 min. In parallel, LN slices were collected from naive animals and sliced as described above. For the on-chip condition, the LN slice was added to the filled 2 T device in the downstream well, and the mock skin was loaded on to a removable mesh support and loaded on-chip in the upstream well. For the well plate condition, the LN slice was added to a media-filled well in a 12-well plate, followed by the mock skin next to it. After 6 hours, the LN slices were collected for both the imaging experiment and the RNA sequencing experiment.

Immunostaining and confocal fluorescence microscopy for vaccination experiment

Upon collection, all slices were immunostained as described previously.[80] Briefly, slices were blocked with anti-mouse CD16/32 for 30 min in a cell culture incubator. An antibody cocktail containing BV421 CD86, AF488 CD69, AF647 CD40, and Starbright Violet 670 CD19 was added for 1 h (Table S1†). Prior to imaging, the slices were washed for 30 min in 1× PBS. Confocal microscopy was performed on a Nikon A1Rsi confocal upright microscope using 405, 487, 561, and 638 nm lasers paired with 450/50, 525/50, 525/50, and 685/70 nm PMTs on a GaAsP detector, respectively. Starbright Violet 670 was excited off the 405 nm laser and detected with the 685/70 PMT. Images were collected with a 40×/0.45NA Plan Apo NIR WD objective.

Images were analyzed using ImageJ (version: vt1. 53 t). Three regions of interest (ROIs), the entire slice, CD19+, and CD19− region, were defined by thresholding the outline of the tissue or the CD19 signal in the Cy5 channel. In each ROI, the mean gray value (MGV) of CD86, CD69 and CD40 were quantified. Each image was corrected for spillover from other channels by subtracting average MGV from three fluorescent minus one (FMO) images. The reported results are pooled from three identical experiments performed on different days.

RNA isolation and sequencing

RNA was isolated from intact LN tissue and slices using the RNeasy Plus Mini (Qiagen, Germany). Samples were kept on ice throughout isolation process and surfaces were cleaned using RNase AWAY (Molecular BioProducts, California, USA). For both R848 + Rho-OVA and PBS *in vivo* conditions, each sample consisted of 2 intact LNs from a single mouse. For both R848 + Rho-OVA and PBS well plate and on-chip conditions, each sample consisted of 3 pooled LN slices from a single mouse. A sample key can be found in Table S2.†

Intact LNs or LN slices removed from agarose were placed in 350 μL of RLT buffer with 1% 14.3 M ß-mercaptoethanol (Sigma-Aldrich, Missouri, USA) and homogenized using a Model 150 VT Ultrasonic Homogenizer (BioLogics, Inc., North Carolina, USA) at 30% power for 7 pulses over 2 min, then vortexed at maximum speed for 1 min. The samples were centrifuged for 3 min at maximum speed. The supernatant was transferred to a gDNA Eliminator spin column in a 2 mL collection tube and centrifuged for 30 s at 8000 × *g* to remove DNA from the sample. The column was discarded, and 350 μL of 70% ethanol was added to the flow-through and mixed. The 700 μL of sample was added to a RNeasy spin column placed in a 2 mL collection tube and centrifuged for 15 s at 8000 × *g* and the flow-through was discarded. Next, 700 μL of RW1 buffer was added to the spin

Open Access Article. Published on 02 December 2024. Downloaded on 5/13/2026 2:24:47 PM. This article is licensed under a Creative Commons Attribution-NonCommercial 3.0 Unported Licence.

column and centrifuged for 15 s at 8000 × *g* and the flow-through was discarded. 500 μL of RPE buffer was added to the spin column and centrifuged for 15 s at 8000 × *g* and the flow-through was discarded. Another 500 μL of RPE buffer was added to the spin column and centrifuged for 2 min at 8000 × *g*. The spin column was placed in a new 2 mL collection tube and centrifuged for 1 min at full speed to eliminate residual buffer. To elute the RNA, the spin column was placed in a new 1.5 mL collection tube and 50 μL of RNase-free water was added directly to the spin column membrane. The spin column and 1.5 mL tube were centrifuged for 1 min at 8000 × *g* to elute the RNA.

Following RNA isolation, the sample purity and concentration were measured using a ND-1000 NanoDrop spectrophotometer (Thermo Fisher Scientific, Massachusetts, USA). All samples per condition from a single experiment were pooled to improve RNA yield, where two samples from different mice were pooled for every experiment. After pooling, six samples remained (*in vivo* R848 + Rho-OVA, *in vivo* PBS, well plate R848 + Rho-OVA, well plate PBS, on-chip R848 + Rho-OVA, and on-chip PBS), with each sample containing RNA from multiple experimental and biological replicates (Table S5†). The experiment was run in triplicate and all samples were stored at −80 C until sequenced. The RNA samples were submitted to NovoGene Co (California, USA) for sequencing. Following quality control, a non-directional low-input eukaryotic mRNA library was prepared. Bulk RNA sequencing was performed using a NovaSeq PE150 with 6 G of raw data per sample.

Bioinformatics analysis

The RNA-seq data analysis was done by the University of Virginia Bioinformatics Core (RRID: SCR_012718). On average, 22 million (ranges from 21 to 27 million) paired end reads (150 bases long read) were received for each of the replicates sufficient for gene level quantitation. The read quality was assessed using the fastqc program (**https://www.bioinformatics.babraham.ac.uk/projects/fastqc/**), and raw data quality report was generated using the MultiQC tool.[81] Adaptor contamination observed in few samples were removed using "cutadapt" program.[82] The "splice aware" aligner 'STAR' aligner was used for mapping the reads.[83] Prior to mapping, a mouse reference index was constructed based on the GRCm38 mouse genome reference (Mus_musculus.GRCm38.dna.primary_assembly.fa & Mus_musculus.GRCm38.91.chr.gtf), and the sjdbOverhang parameter was set to 149 to match the read length of the samples. Subsequently, read mapping and quantification were conducted; more than 95% of the reads mapped to mouse genome and transcriptome.

Gene-based read counts were derived from the aligned reads, and subsequently, a count matrix was generated, serving as the input file for the analysis of differential gene expression. The DESeq2 package was used to conduct the differential gene expression analysis.[84] Low expressed genes (genes expressed only in a few replicates and with low counts) was excluded from the analysis before identifying differentially expressed genes. Data normalization, dispersion estimates, and model fitting (negative binomial) were carried out with the DESeq function.

The log-transformed, normalized gene expression of 500 most variable genes was used to perform an unsupervised principal component analysis. The differentially expressed genes were ranked based on the log 2-fold change and FDR-corrected p-values. Principal component analysis, *z* score heatmap, and gene set enrichment analysis (GSEA) for Hallmark pathways were carried out in R with the following three comparisons: 1) *in vivo* R848 + Rho-OVA/*in vivo* PBS, 2) on-chip R848 + Rho-OVA/on-chip PBS, and 3) wells R848 + Rho-OVA/wells PBS. Pathway analysis was performed using fgsea package in Bioconductor R (**https://bioconductor.org/packages/release/bioc/html/fgsea.html**). The reference database for mouse pathway enrichment analysis comprised Hallmark gene sets from the msigdb.[85–87]

Results and discussion

Customizable multi-compartment 3D-printed platform

The major design goals when designing the multi-compartment chip were 1) fast and reproducible fabrication; 2) expandable design to accommodate the co-culture of two or more tissues; 3) easy tissue insertion and removal for timecourse imaging without tissue damage; 4) biocompatibility with tissue slice culture; and 5) recirculating fluid flow on-chip. Inspired by the principles of our previous PDMS prototype,[27] we developed a monolithic 3D-printed device that consisted of a loop of channels that connected varying numbers of tissue culture wells. The culture wells were in line with a pump well[75] for recirculation of media and secreted molecular cues (Fig. 1b–d). The use of resin 3D printing provided a semi-transparent, easily customizable device. This fabrication method enabled complex 3D architectures such as sloped channels and mesh supports for slice culture, which would be challenging to produce using traditional soft lithography fabrication.[75,88] We designed a series of monolithic devices with zero to four culture wells (0T–4T) to illustrate the flexibility of the platform while retaining its simplicity (Fig. 1e), each printing in <1 h. Users may select the device that is best suited for their specific application, based on the intended number of culture chambers. The multi-compartment chips had 500 μm channels for reproducible fabrication on the printer used; this is larger than most lymphatic vessels and veins. In the future, channels could be made smaller by using different liquid resin formulations and higher resolution printers.[77,89–92]

In principle, this system is compatible with 2D, 3D, or explant cultures inserted into the culture wells. Here, we incorporated live LN tissue slices to maintain the spatiotemporal organization of this organ and make it accessible for imaging and stimulation.[27,68,93] Tissue slices are often cultured using perfusion to increase nutrient and gas exchange, and slices have a long history of incorporation into microscale perfusion devices.[27,63,93–102] Here, to allow the fragile slices to be easily added on demand and removed

 This journal is © The Royal Society of Chemistry 2025

Open Access Article. Published on 02 December 2024. Downloaded on 5/13/2026 2:24:47 PM.
This article is licensed under a Creative Commons Attribution-NonCommercial 3.0 Unported Licence.

repeatedly for timecourse imaging, slices were placed on a removable mesh support (Fig. 1c and S1†), which could be quickly removed from the device using standard tweezers. Unlike commercially available transwell inserts with tall plastic walls, the 3D-printed removable mesh was of a depth to hold the tissue between the channel inlet at the top of the chamber and outlet at the bottom of the chamber, thus providing transverse flow to carry signals downstream. We incorporated gaps in the mesh support around the edge of the tissue slice to limit the resistance through the fluidic loop.[27]

Compact, tubing-free impeller pump and motor-based pump platform

Most standard pumps and pneumatic pressure controllers are bulky or incompatible with cell culture incubators, and thus require long tubing that is prone to bubbles, contamination, or disconnection. To avoid these issues, we developed a companion impeller pump with the following major design criteria: 1) no tubing, few wires, and simple controls for ease of use; 2) tunable recirculating fluid flow; 3) minimal media volume to reduce dilution; 4) low cost; 5) small footprint; and 6) low heat output. To achieve the first two criteria, the tubing-free impeller pump was driven by magnets rotated by a small DC motor inside a custom electronic control box totaling to ~$35 (Fig. 2a and b). The pumps fit eight per row (Fig. 2c) for a theoretical total of 48 pumps per incubator. The spinning magnets drove the rotation of a magnetic impeller on-chip to generate recirculating fluid flow in the connecting channel loop (Fig. 2d and Movie S1†). For simplicity, here we used commercially available stir bars of different sizes as

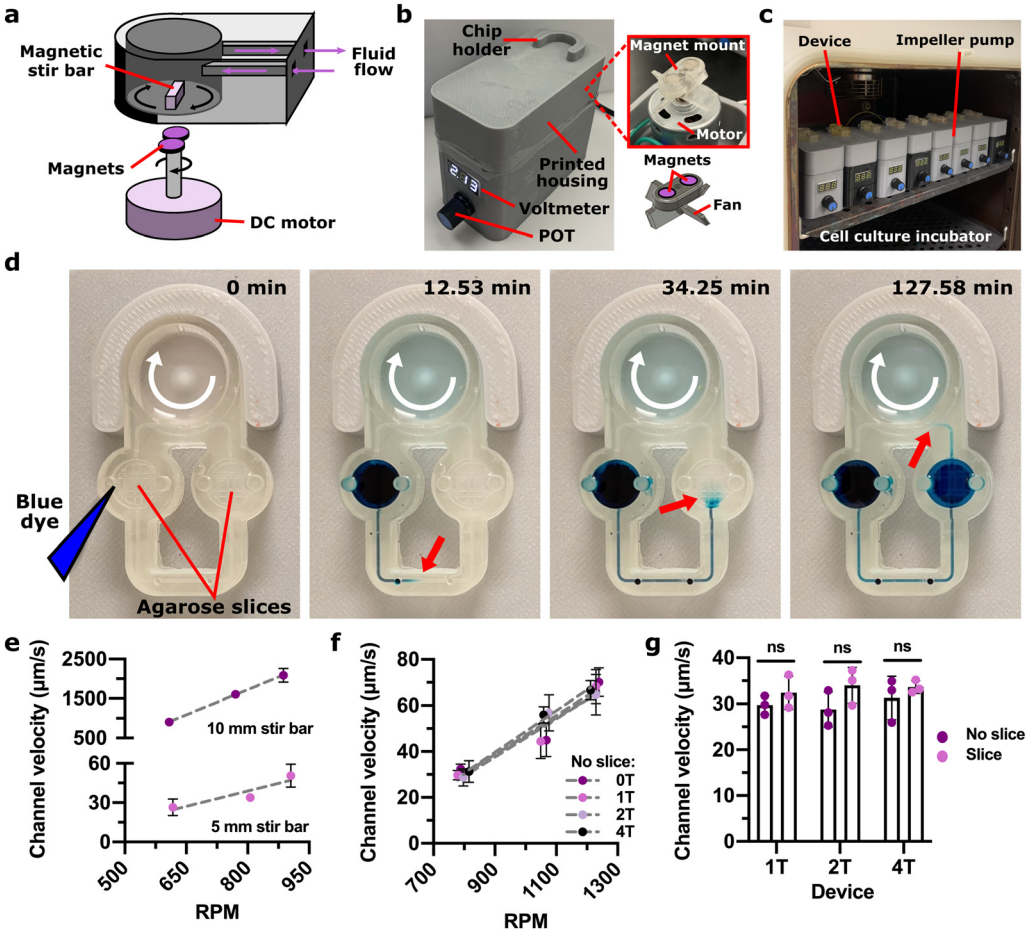

Fig. 2 Motor-based impeller pump for fluid flow recirculation and control on-chip. (a) Schematic of the approach for impeller rotation. (b) Photos of the pump platform showing the outside of the pump box and (*right*) the interior of the pump. (c) Photo of eight impeller pumps on a shelf in a standard cell culture incubator, each holding a single multi-compartment chip. (d) Time-lapse images of recirculating fluid flow on a 2 T device (clear resin) with an agarose slice in each well (5 mm stir bar, 1000 RPM). Blue dye was inserted in the upstream culture well, and over time, moved through the channel to the downstream culture well and then the pump well (dye front marked with red arrow). The stir bar rotated clockwise within the pump well (white arrow). (e and f) Experimentally measured maximum velocity within the channel in (e) a 0 T device (no culture wells) using a 10 mm stir bar and a 5 mm stir bar, and (f) in varied device designs (0–4 T) with a 5 mm stir bar, all with no slice added. Dots and error bars represent mean and standard deviation; some error bars too small to see. (g) Experimentally measured maximum velocity in the channel at a low RPM (1.2 V, 780 RPM; 5 mm stir bar), with and without the addition of an agarose slice in each device. Each dot represents one velocity measurement. Results were compared using an unpaired *t*-test (n = 3). ns indicates $p > 0.1$.

Open Access Article. Published on 02 December 2024. Downloaded on 5/13/2026 2:24:47 PM.
This article is licensed under a Creative Commons Attribution-NonCommercial 3.0 Unported Licence.

impellers; in past work, we have also used 3D-printed cross-shaped impellers[75] and vaned impellers successfully (unpublished results). With the motor and stir bar, the fluid volume in the chip was reduced by >2-fold and the footprint of the pump reduced by 2-fold compared to an earlier prototype.[75] We confirmed that the stir bar revolutions per minute (RPM) increased linearly with voltage (Fig. S2a†) and was stable for 90 h (Fig. S2b†).[75] In a 10-day test of heat output by 8 pumps, temperatures in the incubator remained within the acceptable range (±1 deg) (Fig. S2c†).[103]

On-chip fluid recirculation at controllable speeds

We made use of this pump to recirculate media and secreted factors through the chip for communication between culture compartments, rather than to specifically model the geometry or shear rates of human or mouse vasculature. As flow velocity is a critical parameter, we tested how well the chip and pump achieved a range of flow regimes, ranging from μm s^{-1} to mm s^{-1}. We previously showed that channel velocity was controlled by the physical geometry of the chip (*e.g.* channel width and length and pump well geometry).[75] Here, we quantified the velocity through a fixed chip geometry as a function of user-controllable parameters. Doubling the length of the stir bar from 5 to 10 mm increased the channel velocity from tens of μm s^{-1} to mm s^{-1}, respectively, thus providing access to different flow regimes (Fig. 2e). Varying the volume of fluid added to the device also tuned the channel velocity, with reduced speeds as the meniscus rose away from the entry point of the channel (Fig. S3a and b†). On the other hand, channel velocities were comparable between each device variation (0

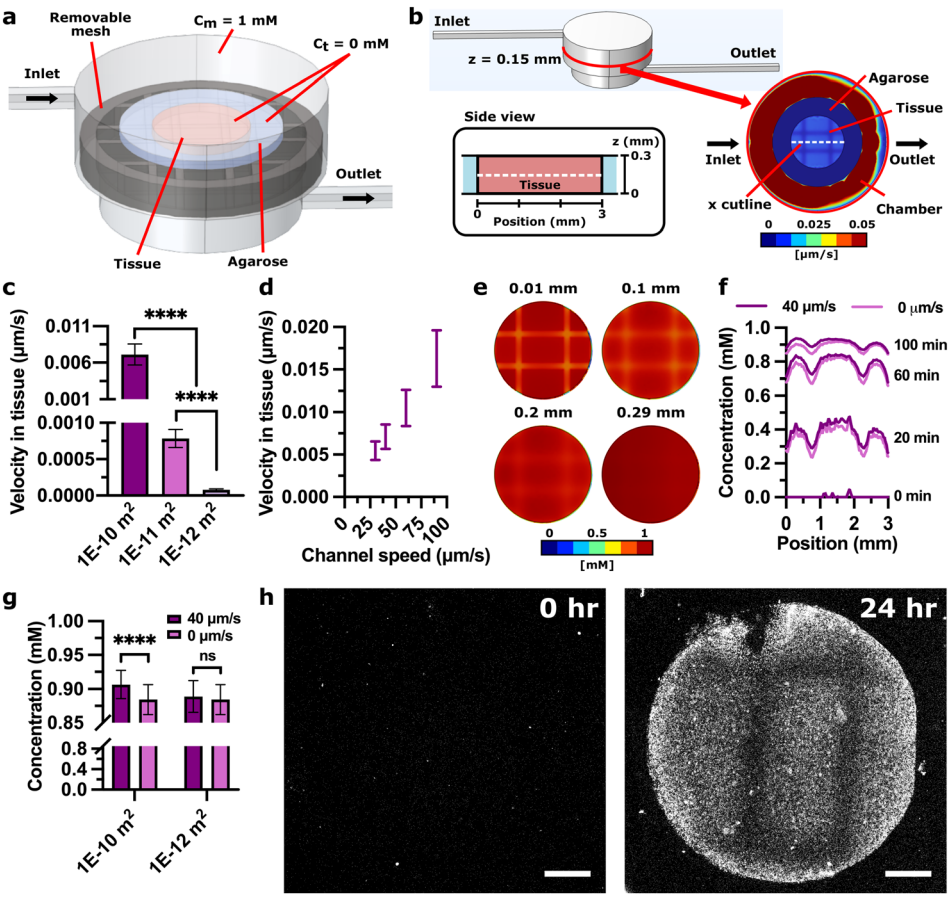

Fig. 3 Simulated fluid velocity and tracer concentration through a tissue slice. (a) Geometry of the 3D COMSOL simulation, colored to show the tissue (*pink*) embedded in agarose (*blue*) resting on the removable mesh support (*dark gray*). The inlet channel intersects the top of the culture well, while the outlet channel intersects the bottom on the opposite side. (b) The velocity and tracer concentration were measured along cutlines along the *x* axis in line with the inlet and outlet channels, at different *z* planes. (c and d) Predicted velocity in tissue for (c) a range of tissue permeabilities at an inlet speed of 30 μm s^{-1} and (d) a range of inlet speeds at a permeability of 1×10^{-10} m^2. One-way ANOVA with Tukey *post-hoc* tests. **** indicates $p < 0.0001$. In d, the error bars represent the range of velocity along the cutline. (e) Color plots of protein concentration in the tissue domain at 100 min at a permeability of 1×10^{-10} m^2, showing different *z* planes (mm). (f) Predicted protein concentration in tissue over time with flow (40 μm s^{-1}) and without flow (0 μm s^{-1}) at a tissue permeability of 1×10^{-10} m^2 on a central cutline (z = 0.15 mm) (g) predicted protein concentration in tissue as a function of tissue permeability and flow on a central cutline (z = 0.15 mm) at 100 min. Bars represent standard deviation. One-way ANOVA with Tukey post-hoc tests. **** indicates $p < 0.0001$, ns indicates $p > 0.2$. (h) Representative images of the effect of the mesh support in a physical device (not simulated), showing NRho (white) that was captured within the biotin region of the agarose slices at 0 h and 24 h, in a chip operated at a channel speed of 30 μm s^{-1}. Scale bar shows 500 μm.

 This journal is © The Royal Society of Chemistry 2025

Open Access Article. Published on 02 December 2024. Downloaded on 5/13/2026 2:24:47 PM. This article is licensed under a Creative Commons Attribution-NonCommercial 3.0 Unported Licence.

T, 1 T, 2 T, and 4 T) (Fig. 2f) and with and without agarose slices added (Fig. 2g). Thus, at least with the current mesh support, the culture wells and mock tissue slices did not significantly increase the resistance of the microfluidic loop, providing robust flow control through the channels at wide ranges of fluid flow regimes.

Tissue permeability and channel velocity control interstitial fluid speeds and soluble factor delivery in 3D computational model

Next, we determined the predicted range of interstitial flow rates and the spatial distribution of mass transport through the tissue compartment. Interstitial flow rates *in vivo* vary widely, with typical estimates ranging from 0.01–10 μm s^{-1}.[104–106] In a pressure-driven system, the hydraulic permeability of the tissue has a major impact on expected interstitial flow rate.[53,105] To capture these effects, we developed a 3D finite element model of the tissue in the culture well using COMSOL Multiphysics (Fig. 3a and b, see ESI† Methods). The simulated tissue and agarose were placed atop an impermeable mesh support and modeled as porous matrices of defined permeability and porosity. The permeability of the lymph node will significantly impact the interstitial fluid flow and molecular transport in the tissue, but this feature is largely unmeasured. Here, we tested the range of available predictions for LN permeability from 10^{-10} to 10^{-12} m^2.[53,107]

With the current mesh geometry, we anticipated that most of the fluid would pass through the gaps in the mesh support rather than through the tissue (illustrated in Fig. 1c). Indeed, only when the simulated tissue was more permeable (1×10^{-10} m^2) did the mean interstitial flow velocities overlap with the lower bound of physiological interstitial fluid flow, ranging from 0.006 to 0.02 μm s^{-1} as a linear function of channel speed (Fig. 3c and d and S4a†). Tissues with lower permeabilities had negligible interstitial fluid flow.

In addition to velocity, we investigated the shear stress in the tissue and in the channels. Based on the computational model, we found that at a channel speed of 40 μm s^{-1}, the predicted shear stress through the tissue was $<3 \times 10^{-6}$ dyn cm^{-2} (Fig. S5a†), well below physiologically relevant shear stress ranging from 0.1 to 70 dyn cm^{-2},[108–110] and thus was not expected to impact tissue viability significantly. Within the channels of the device, the shear stress was predicted to be 0.0005–0.0035 dyn cm^{-2} (Fig. S5b†). In the future, it may be possible to increase the velocity and shear stress within the tissue to within physiologically relevant ranges by reducing the open space around the mesh, increasing the channel speed, or increasing the viscosity of the cell culture medium.

As one of the key functions of a multi-compartment chip is to transport molecular cues from the media into each tissue, we assessed the distribution of their penetration into the tissue domain. As expected, the tracer concentration (Fig. 3e–h and S4b†) was lower in the regions directly above the bars of the mesh support. Fluid flow had a minimal impact on tracer distribution (Fig. 3f) and mean concentration (2.5% increase; Fig. 3g), even at a high tissue permeability (1×10^{-10} m^2). Uniformity increased at greater z planes further from the mesh and over time due to diffusion, evident by the 3-fold decrease in standard deviation (Fig. 3e). To test the predictions of distribution experimentally, we loaded a device with a slice of agarose embedded with biotinylated beads and injected a fluorescently-labeled soluble ligand (NeutrAvidin Rhodamine Red-X, or NRho) into the recirculating media.[27] As predicted by the COMSOL model, the ligand reached the majority of the sample, with more protein delivered through the open regions of the mesh (Fig. 3g). In the future, area of the crossbars can be minimized or rearranged as needed, or customized membrane inserts may be used instead.

Lymph node tissue slices remain viable for 24 h culture under recirculating flow on-chip

Next, we tested for any impact of recirculating flow or co-culture on viability of tissues on the 3D-printed chip, focusing on *ex vivo* lymph node slices because of the intended application of vaccination and because leukocytes are highly sensitive to their environment. Indeed, resin 3D-printed materials fabricated from commercially available resins are highly cytotoxic to primary murine splenocytes.[75,88] However, we recently showed that coating the materials with a layer of Parylene C, a method commonly used for medical implants and hardy cells in 3D-printed chips,[111–114] was sufficient to protect splenocytes for at least 24 h.[78] Here, we confirmed that parylene coating similarly restored viability of primary LN slices in static culture (Fig. 4a and b). Furthermore, LN slice viability was not significantly impacted by fluid flow on the device (Fig. 4a and c). Due to the heterogeneity of cell number across LN slices, there is a large variation in MTS signal in live samples as the assay is sensitive to number of cells present. We note that although not statistically significant, the high pump speed (75 μm s^{-1}) trended lower in viability than the other conditions, indicating possible damage that should be explored in the future. At the low speed (30 μm s^{-1}), viability was similar whether one or two slices were cultured in the device, and was not different between upstream and downstream culture wells (Fig. 4d). These results confirmed that tissue slices could be cultured in either well and in tandem while maintaining viability.

Two-compartment chip mimics antigen drainage to and processing in lymph node slices

Having established that the chip and pump provided recirculating fluid flow and molecular transport and was compatible with lymph node culture, we sought to use this multi-compartment system to model entry of molecular cues into the LN. *In vivo*, LNs are continually exposed to molecules arriving from upstream tissues, both directly through the draining lymphatics and indirectly *via* the bloodstream. We hypothesized that the multi-compartment chip could

Open Access Article. Published on 02 December 2024. Downloaded on 5/13/2026 2:24:47 PM.
This article is licensed under a Creative Commons Attribution-NonCommercial 3.0 Unported Licence.

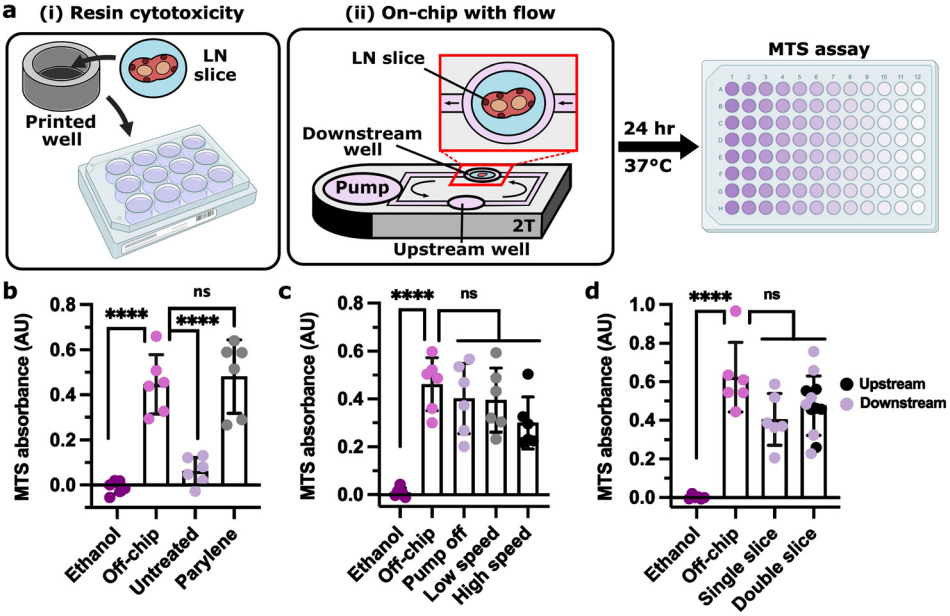

Fig. 4 Lymph node slices were viable for 24 h culture on-chip. (a) Experimental setup for 24 h LN slice viability for (i) resin cytotoxicity and (ii) on-chip culture under fluid flow (well plate images created using **https://BioRender.com**). (b) MTS assay absorbance of LN slices cultured in untreated and parylene-coated 3D-printed wells (clear resin) for 24 h, without fluid flow, compared to live (off-chip) and killed (ethanol) slices cultured off-chip. (c) MTS assay absorbance of LN slices cultured for 24 h on the parylene-coated 2 T device (clear resin) with the pump off, at low speed (1.2 V, 35 μm s^{-1}), or at high speed (1.7 V, 75 μm s^{-1}) compared to live (off-chip) and killed (ethanol) slices cultured off-chip. (d) MTS assay absorbance of LN slices cultured for 24 h on the parylene-coated 2 T device (clear resin) with one or two slices cultured per device at a low pump speed (1.2 V, 30 μm s^{-1}) compared to live (off-chip) and killed (ethanol) slices cultured off-chip. One-way ANOVA with Tukey post-hoc tests (n = 6). **** indicates $p < 0.0001$, ns indicates $p > 0.1$. Bars represent mean and standard deviation. Each dot represents one LN slice. All results pooled from two independent experiments.

approximate the relative dilution that occurs after intravenous (i.v.) injection *versus* subcutaneous (s.c.) or intramuscular (i.m.) injection.[115] To test this hypothesis, we loaded a biotinylated model tissue into one of the culture wells and injected NRho into an upstream compartment that was connected either through the pump well (well first, approximating i.v. injection) or directly through a microchannel (channel first, approximating s.c. or i.m. injection) (Fig. 5a). For the first hour, the channel-first condition had a nearly 10-fold greater rate of capture compared to the well-first condition (Fig. 5b), resulting in a level of signal that it took the well-first condition 24 h to attain. Thus, the device successfully replicated this aspect of the different drainage routes found *in vivo*. Because there was no protein clearance in this system, capture rates were similar after the first hour, and we anticipate that eventually, both conditions would reach equilibrium with comparable protein capture, unlike *in vivo* where molecules are gradually cleared from the body.

Next, we tested the ability of the multi-compartment system to model antigen drainage and processing in *ex vivo* LN slices. We selected DQ-ovalbumin (DQ-OVA) as a model antigen, as it becomes fluorescent only when proteolytically cleaved. DQ-OVA was injected into the upstream culture well to mimic s.c. injection (Fig. 5c) or added to the media in a well plate (off-chip) for comparison. As expected, the DQ-OVA signal increased at a greater rate in live LN slices than in ethanol-treated killed controls (Fig. 5d–g), both on-chip and off-chip, confirming that the live slices remained metabolically active and able to process antigen on-chip. A slow appearance of signal in ethanol-treated slices may have been due to residual protease activity (Fig. 5d);[116,117] we observed similar results in formalin-fixed tissues previously.[68] We note that the DQ-OVA signal magnitude and distribution was variable between different lymph node slices due to the heterogenous cell distributions found in the tissue. Processed antigen was brighter in slices on-chip than off-chip, consistent with better delivery by fluid flow than in static culture. After 24 h, the live slices cultured on-chip showed the mesh support pattern in certain regions (Fig. 5gi), similar to prior tests in mock tissue (Fig. 3g). Nevertheless, processed antigen appeared in similar regions of the lymph node as observed previously, near the outer sinus regions.[68,118] Thus, the multi-compartment chip successfully modeled lymphatic drainage, phagocytosis, and processing of whole protein antigens in a lymph node.

Acute immune response to on-chip vaccination was comparable to *in vivo* vaccination

Within minutes to hours of a vaccine injection, vaccine components drain from the site of injection to local LNs, where an immune response begins to develop.[51] We sought to model these events by vaccinating a mock injection site

 This journal is © The Royal Society of Chemistry 2025

Open Access Article. Published on 02 December 2024. Downloaded on 5/13/2026 2:24:47 PM.
This article is licensed under a Creative Commons Attribution-NonCommercial 3.0 Unported Licence.

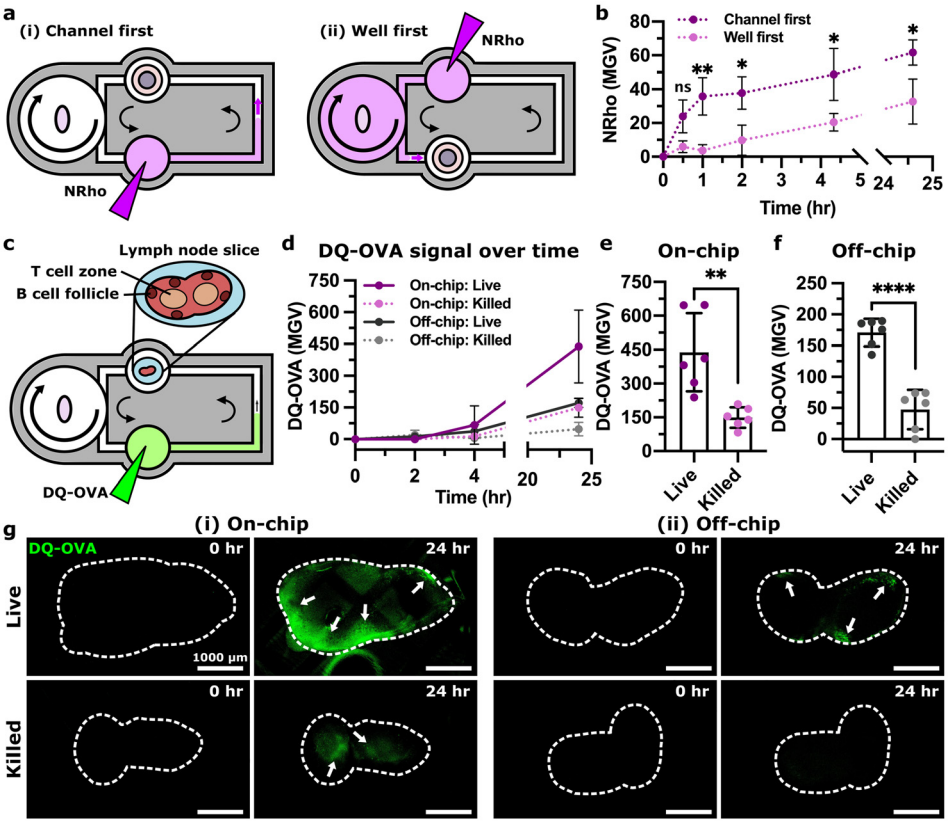

Fig. 5 Modeling antigen drainage and uptake using two-compartment chip. (a) NRho (*purple*) was inserted in a filled 2 T device (uncoated ITX-PEGDA resin) in the (i) channel-first orientation and the (ii) well-first orientation. (b) Quantification of NRho MGV in channel first and well first conditions over time (n = 3). One-way ANOVA with Tukey *post-hoc* tests. ns indicates $p > 0.3$, * indicates $p < 0.03$, and ** indicates $p < 0.007$. Dots and error bars represent mean and standard deviation, respectively. (c) A lymph node slice was inserted in a 2 T device (parylene-coated clear resin, 1.2 V, 30 μm s^{-1}) with a DQ-OVA injection (*green*) in the upstream culture well. (d) Mean gray value (MGV) of DQ-OVA in LN slices over time, showing processing of protein antigen. Dots and error bars represent mean and standard deviation; some error bars too small to see. (e and f) MGV of DQ-OVA in live or ethanol-treated LN slices cultured on-chip or off-chip at 24 h. Unpaired t test (n = 6). **** indicates $p < 0.0001$, ** indicates $p < 0.003$. Each dot represents one LN slice. (g) Representative images of DQ-OVA signal (green) in live and killed slices cultured (i) on-chip and (ii) off-chip at 0 h and 24 h. slices outlined with dashed white line from brightfield images (not shown). Arrows indicate regions that appear to have processed DQ-OVA. All results pooled from two independent experiments.

upstream of a murine LN slice on the multi-compartment chip (Fig. 6ai). As a model vaccine, we chose rhodamine-labeled ovalbumin (Rho-OVA) and R848 (TLR7/TLR8 agonist) as the antigen and adjuvant, respectively. This mixture, or a phosphate-buffered saline (PBS) control, was loaded into a block of soft hydrogel as the mock injection site. The calculated drainage time from the upstream culture well to the downstream culture well was approximately 23 min. To assess the accuracy of the multi-compartment chip and impeller pump platform, we benchmarked the on-chip response to vaccination against the response to s.c. vaccination *in vivo* in mice (Fig. 6aii). Furthermore, we compared the response on-chip to off-chip in static well plates to assess the utility of the chip *versus* conventional culture (Fig. 6aiii).

First, we assessed the early markers of activation after vaccination by confocal microscopy (Fig. S6†), imaging three markers: CD69 for lymphocyte activation, and CD40 and CD86 for antigen-presenting cell (APC) activation. Because CD69 expression increases in LN slices after overnight culture,[119] we restricted the *ex vivo* cultures to 6 h; *in vivo* vaccination was analyzed at a standard time point (24 h). Both on-chip and *in vivo* vaccinations both showed strong induction of CD69, particularly in the CD19+ region, whereas little response was observed in PBS controls (Fig. 6b and c). In contrast, the slices cultured off-chip yielded a smaller and not statistically significant increase in CD69 signal; however, it is not possible with the current data to conclude whether or not static conditions may have led to slower or lesser CD69 protein expression compared to conditions under flow. CD40 and CD86 both had high enough basal expression in PBS controls that vaccination had no impact; this result was consistent between *in vivo*, on-chip, and well plate conditions (Fig. S7†). Despite the difference in time point, antigen distribution also was similar across all three platforms, with Rho-OVA appearing primarily in the sinus region (Fig. 6d).

Next, we compared transcriptomic changes in the LN by bulk RNA sequencing. For simplicity, we maintained the same 6 h time point for all vaccination conditions (Fig. 7a).

Open Access Article. Published on 02 December 2024. Downloaded on 5/13/2026 2:24:47 PM.
This article is licensed under a Creative Commons Attribution-NonCommercial 3.0 Unported Licence.

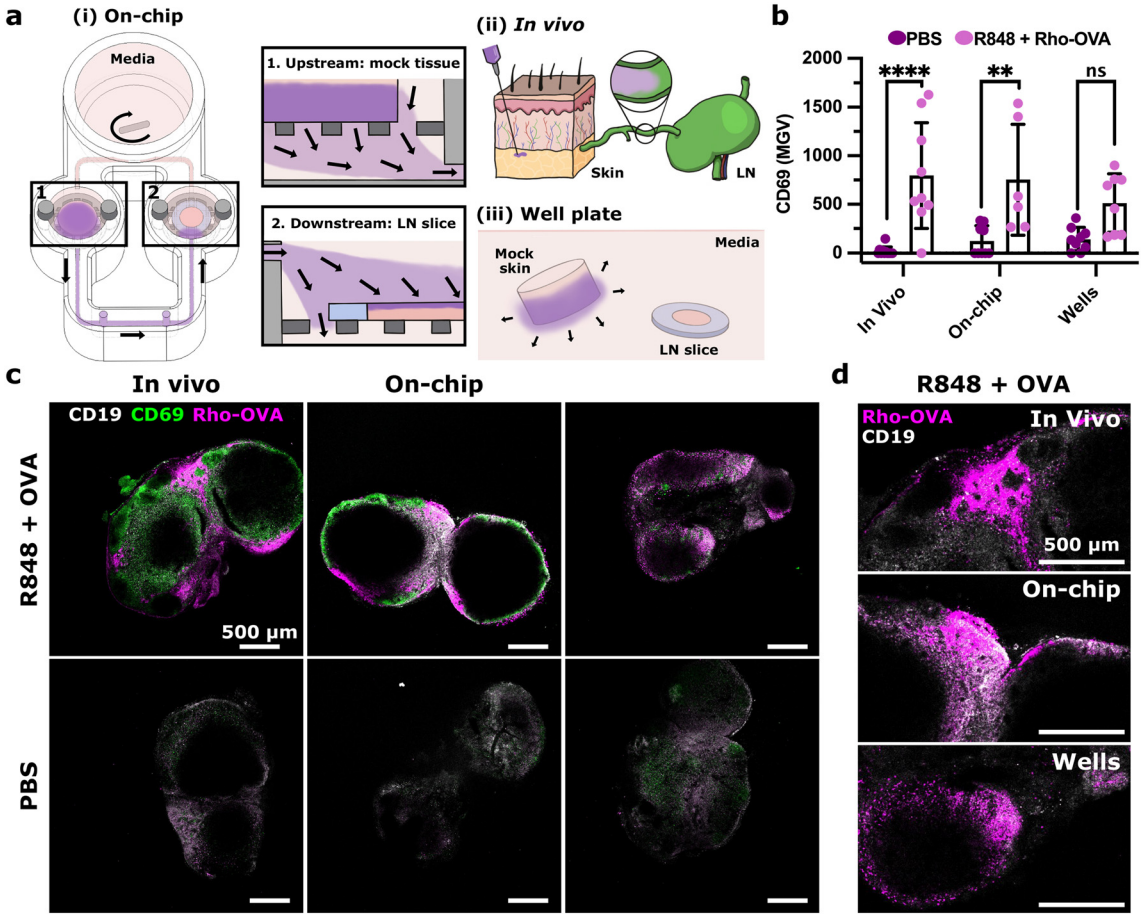

Fig. 6 Similar activation marker signal and antigen distribution upon vaccination in *in vivo* and on-chip conditions. (a) Three vaccination conditions were compared: (i) on-chip in a 2T device (parylene-coated clear resin), (ii) s.c. injection *in vivo*, and (iii) static well plate, where the vaccine is shown in purple. (b) Quantification of the MGV of CD69 in the CD19+ region for all conditions. Results in (e) were pooled from three independent experiments. Two-way ANOVA; **** indicates $p < 0.0001$, ** indicates $p < 0.003$, and ns indicates $p > 0.07$. Each dot represents a single LN slice. Bars represent standard deviation. (c) Representative images of LN slices with R848 + Rho-OVA or PBS from *in vivo* culture, on-chip culture, and well plate culture. B cells (CD19) are shown in gray; CD69 is shown in green; and Rho-OVA is shown in magenta. (d) Representative images of Rho-OVA (magenta) distribution across conditions. B cells (CD19) are shown in gray.

Principal component analysis (PCA) separated the vaccinated (R848 + Rho-OVA) and unvaccinated (PBS) conditions along PC2, although as a smaller effect than the separation between *in vivo* lymph nodes and *ex vivo* lymph node slices on-chip or in wells along PC1 (Fig. 7b). In future experiments, it would be preferable to slice the lymph nodes from the *in vivo* condition as well, as slicing likely impacted both gene expression and RNA yield. Nevertheless, heatmap analysis showed similar changes in gene expression after vaccination on-chip as *in vivo* or in well plates (Fig. 7c). Consistent with the earlier immunofluorescence staining (Fig. 6b), cd69 expression increased upon vaccination across all three conditions (Fig. 7di). Interestingly, cd40 expression also increased in all conditions (Fig. 7dii) and cd86 increased *in vivo* (Fig. S8†), which were not detectable by immunofluorescence (Fig. S7b and c†). As expected during an antiviral immune response,[120,121] expression of genes such as ifng, tnf, and cxcl9 increased (Fig. 7diii–v) and decreased for il9r, a receptor for a cytokine commonly associated with an anti-inflammatory immune response (Fig. 7dvi).[122] These changes were similar across all three conditions.

Gene set enrichment analysis (GSEA) showed that both on-chip and well plate conditions shared eight of the top ten positively enriched pathways with the *in vivo* condition (Fig. 7e–g, Table S3–S5†). In fact, all conditions shared the same top four positively enriched pathways consistent with an early vaccine response: IFNγ response, IFNα response, MYC target V1, and MYC target V2. Of the top three negatively enriched pathways, on-chip and well plate conditions each shared one pathway with the *in vivo* condition.

Overall, the multi-compartment chip provided vaccine drainage and initial immune responses in the LN that were comparable to *in vivo* vaccination in terms of spatial distribution of antigen and activation markers as well as several of the most enriched gene expression pathways. Off-chip treatment of LN slices with this particular vaccine also produced a similar response, showing that in some cases, LN slices may be sufficient

 This journal is © The Royal Society of Chemistry 2025

Open Access Article. Published on 02 December 2024. Downloaded on 5/13/2026 2:24:47 PM.
This article is licensed under a Creative Commons Attribution-NonCommercial 3.0 Unported Licence.

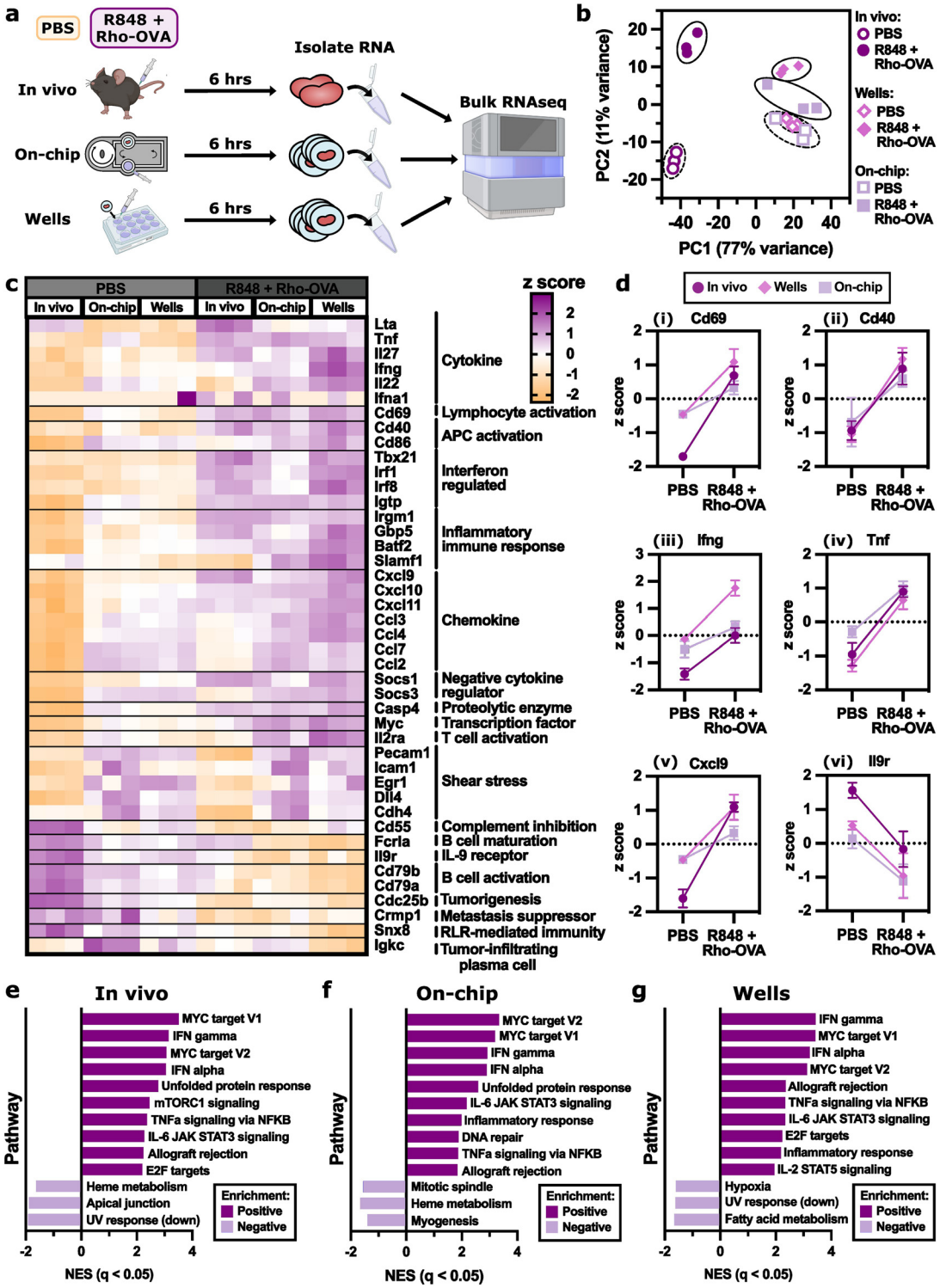

Fig. 7 On-chip vaccination induced similar differentially expressed genes compared to *in vivo* vaccination. (a) Schematic showing RNA sequencing experimental workflow. For the *in vivo* condition, naive mice were injected s.c. with either PBS or R848 + Rho-OVA. After 6 h, the skin-draining lymph nodes were collected and the RNA was isolated from intact nodes before sequencing. For well and on-chip conditions, skin-draining lymph nodes from naive mice were first sliced then cultured *ex vivo* in a well plate or on the 2 T device with either PBS or R848 + Rho-OVA. After 6 h, RNA was isolated from the tissue slices before sequencing. Tubes and RNAseq instrument images created using **https://BioRender.com**. (b) Principal component analysis (PCA) of the normalized gene expression data, where the percent variance explained by each PC is listed in the axis labels. Colors and symbols represent different culture conditions (*in vivo*, on-chip, and wells) with either PBS and R848 + Rho-OVA. (c) Heatmap showing the expression of 36 selected genes of relevance to an immune response, where the cell value is the normalized *z* score. (d) The change in *z* score with the addition of R848 + Rho-OVA across *in vivo*, on-chip, and wells for (i) cd69, (ii) cd40, (iii) ifng, (iv) tnf, (v) cxcl9, and (vi) il9r. (e–g) Enriched pathways from the Hallmark gene set for (e) *in vivo*, (f) on-chip, and (g) wells comparing R848 + Rho-OVA to PBS (Table S3–S5†). The top 10 positively enriched pathways and the top 3 negatively enriched pathways are shown for each condition with $q < 0.05$.

Open Access Article. Published on 02 December 2024. Downloaded on 5/13/2026 2:24:47 PM.
This article is licensed under a Creative Commons Attribution-NonCommercial 3.0 Unported Licence.

without the multi-organ culture platform. However, for vaccination conditions that require events to take place at a physically removed injection site, we expect that the multi-organ system will prove essential.

Conclusions

Here, we have reported a user-friendly, 3D-printed multi-compartment chip and tubing-free impeller pump for the culture of one or more tissue models under recirculating fluid flow. In this system, users may simply pipet media into the chip, load their tissues, and plug in a small, inexpensive control box, bypassing the need for peristaltic or syringe pumps. To replicate activity in spatially organized tissues such as the LN, we designed the device to support live *ex vivo* tissue slices, although the device is also compatible in principle with 3D cultures. By connecting murine or mock tissue slices using recirculating fluid flow, the multi-compartment chip modeled drainage of a vaccine from an upstream injection site to a downstream LN slice. On-chip vaccination yielded similar distribution of antigen, location and intensity of activation markers by immunofluorescence, and gene-specific expression patterns compared to *in vivo* vaccination.

Unlike static or mixed culture models, a strength of the 3D-printed chip and pump platform is that it spatially compartmentalizes the events of an upstream organ compartment from those in a downstream compartment, with communication only *via* the media. As with other compartmentalized multi-organ chip systems, fluidic coupling of physically separated cultures will be important when modeling systemic effects of local events.[8,12,14,123] In the context of lymph node communication, applications may include models of depot vaccination, tissue-specific infection, and local inflammation.

This multi-compartment chip and impeller pump are not without limitations. The current removable mesh geometry yielded little interstitial fluid flow or shear through the tissue itself. The predicted interstitial flow rates were 0.006–0.02 μm s^{-1} at channel speeds of 30–90 μm s^{-1}, compared to the typical expected *in vivo* range of 0.01–10 μm s^{-1}.[104,124,125] As a result, the shear stress through the tissue at approximately 10^{-6} dyn cm^{-2} was orders of magnitude lower than the estimates that exist for lymph node, which range from 0.005 to 0.05 dyn cm^{-2}.[59,124,126] To achieve higher interstitial flow rates and shear stress, the most critical change would be to alter the geometry of the removable mesh to reduce the width of the gaps around the slice. The channel speed could also be increased. Both of these adjustments are easily achievable with the current impeller pump and chip design, though too fast of flow may risk damaging the fragile tissue slices. Alternatively, to increase shear independently of interstitial flow, the media viscosity could be increased from the current value of ~1 mPa·s in complete media with 10% FBS at 37 °C, to a greater value such as that of lymphatic fluid (~1.8 mPa·s)[127] or blood (3.5–5.5 mPa·s).[128]

Outside of the tissue, shear stress in the channels was similarly low, as their 500 μm width was greater than that of human capillaries and mouse blood vessels *in vivo*.[129] To increase the shear stress within the channels, the dimensions of the channels should be made significantly smaller. For example, at a channel velocity of 75 μm s^{-1}, the channels would need to be <10 μm in width and height to achieve a shear stress of 0.5 dyn cm^{-2}. Such a size is beyond the current resolution of resin 3D printing with commercial SLA or DLP printers. As the resin 3D printing field continues to progress, higher resolution printers and smaller, biologically relevant internal channel sizes may become routinely available.[77,91,92] Alternatively, fabrication of the chip by injection molding or CNC machining would improve scalability and resolution.

Here we focused primarily on using flow for simple mass transfer between compartments. Future work will be needed to address organ-to-organ scaling and to model vasculature if required for particular applications.[130–134] The volumes and channel lengths could be adjusted in the future to enable proper organ-to-organ scaling depending on the requirements of the modeled system.[8,130–134] A benefit of fabrication *via* 3D printing is that the system is adaptable, so the user can adjust geometries and features as needed within the resolution of their printer.

Finally, further work is needed to ensure that the rotation of the stir bar does not negatively impact recirculating lymphocytes. Lymphocyte recirculation will be an important design feature for many future applications to multi-organ immunity, although it was not required for the model developed here. With the current use of a rod-shaped stir bar, we observed loss of viability of primary murine splenocytes following 24 h of on-chip recirculation, likely due to high shear from the rotating stir bar (unpublished observations). In addition to slower rotational speeds, alternative impeller designs such as those used in cardiac impeller pumps may prove useful here and are an area of active investigation in our laboratory.[135,136] Furthermore, although we suspect that the parylene coating will retain biocompatibility for 7+ days based on prior reports,[112–114] culture times longer than 24 h will need to be confirmed with lymphocytes or LN slices.

While the current platform generated a similar short-term response to vaccine compared to *in vivo*, there are many features of vaccination to expand on in future work. Currently, LN slices are best used for less than 24–48 h, after which lymphocytes begin to egress, at least in static cultures.[68] In the future, adjustments to culture conditions to enable longer culture times for LN slices, or incorporation of 3D cultured models instead of tissue slices, may enable models of longer-term responses to vaccination. Excitingly, the two-compartment system may enable incorporation of depot adjuvants and tissue-resident APCs into the upstream injection site, thus generating microphysiological models of clinically relevant vaccines such as those adjuvanted with aluminum salts. In the future, this platform can be used to

 This journal is © The Royal Society of Chemistry 2025

Open Access Article. Published on 02 December 2024. Downloaded on 5/13/2026 2:24:47 PM. This article is licensed under a Creative Commons Attribution-NonCommercial 3.0 Unported Licence.

model multi-tissue immunity by co-culturing a LN slice with additional upstream tissues. Beyond vaccination, we envision that this user-friendly, multi-compartment system will be compatible with additional tissue models to predict the progression of other complex phenomena including neurodegeneration, autoimmunity, and tumor immunity.

Data availability

The data generated in this study, including source data for the figures and all device and pump design files are posted under Cook *et al.* "Replication Data for: A 3D-printed multi-compartment organ-on-chip platform with a tubing-free pump models communication with the lymph node," at **https://dataverse.lib.virginia.edu/dataverse/PompanoLab**. The RNAseq data generated in this study is available through NCBI GEO using the accession GSE268137.

Author contributions

SRC and RRP conceptualized the technology, planned experiments, interpreted data, and wrote the manuscript. SRC designed and fabricated the technology, performed the experiments, and analyzed the data. AGB contributed to the design and performance of vaccination experiments, including *in vivo* vaccination and related image analysis. AM led the analysis of RNAseq data through the Bioinformatics Core. All authors edited and approved the final manuscript.

Conflicts of interest

SRC and RRP are listed as inventors on two patent applications (Serial No. 63/080320 and 63/543893) filed by the University of Virginia related to the impeller pump technology and multi-tissue culture.

Acknowledgements

The authors thank Kirk Bryson (Shared Materials Instrumentation Facility, Duke University) for his assistance and helpful correspondence. The authors thank Pankaj Kumar (Bioinformatics Core Facility, University of Virginia, RRID: SCR_012718) for his assistance with RNAseq data analysis and helpful correspondence. The authors thank Hannah Musgrove for technical assistance with cell culture preparation, printing devices, and running initial viability experiments. The authors thank Geane Miranda for technical assistance with printing devices and pump assembly, Alyssa Montalbine for technical assistance with printing devices, Erin Lawrence for technical assistance with LN slicing and editing support, and Meredith Harris for editing support.

Research reported in this publication was supported by the National Institute of Allergy and Infectious Diseases of the National Institute of Health under Award Number R01AI174207 and R01AI131723. The content is solely the responsibility of the authors and does not necessarily represent the official views of the National Institutes of Health. SRC was supported in part by the 2021 Presidential Fellowship for Collaborative Neuroscience from the UVA Brain Institute, the 2022 Sidney M. Hecht Graduate Fellowship from UVA Chemistry, and a 2021 Research Grant from UVA Graduate School of Arts and Sciences Committee (GSASC). Parylene coating was performed at the Duke University Shared Materials Instrumentation Facility, a member of the North Carolina Research Triangle Nanotechnology Network, which is supported by the National Science Foundation (Award ECCS-2025064) as part of the National Nanotechnology Coordinated Infrastructure.

References

1 J. Castillo-Armengol, L. Fajas and I. C. Lopez-Mejia, Inter-organ communication: a gatekeeper for metabolic health, *EMBO Rep.*, 2019, **20**, e47903.
2 J. Hübner, M. Raschke, I. Rütschle, S. Gräßle, T. Hasenberg and K. Schirrmann, *et al.*, Simultaneous evaluation of anti-EGFR-induced tumour and adverse skin effects in a microfluidic human 3D co-culture model, *Sci. Rep.*, 2018, **8**, 15010.
3 E. M. Wasson, K. Dubbin and M. L. Moya, Go with the flow: modeling unique biological flows in engineered *in vitro* platforms, *Lab Chip*, 2022, **2**(33), DOI: **10.1039.D1LC00014D**.
4 J. H. Hammel, S. R. Cook, M. C. Belanger, J. M. Munson and R. R. Pompano, Modeling Immunity *In Vitro*: Slices, Chips, and Engineered Tissues, *Annu. Rev. Biomed. Eng.*, 2021, **23**, 461–491.
5 K. Ronaldson-Bouchard and G. Vunjak-Novakovic, Organs-on-a-Chip: A Fast Track for Engineered Human Tissues in Drug Development, *Cell Stem Cell*, 2018, **22**, 310–324.
6 D. E. Watson, R. Hunziker and J. P. Wikswo, Fitting tissue chips and microphysiological systems into the grand scheme of medicine, biology, pharmacology, and toxicology, *Exp. Biol. Med.*, 2017, **242**, 1559–1572.
7 L. Boeri, L. Izzo, L. Sardelli, M. Tunesi, D. Albani and C. Giordano, Advanced Organ-on-a-Chip Devices to Investigate Liver Multi-Organ Communication: Focus on Gut, Microbiota and Brain, *Bioengineering*, 2019, **6**, 91.
8 N. Picollet-D'hahan, A. Zuchowska, I. Lemeunier and S. Le Gac, Multiorgan-on-a-Chip: A Systemic Approach To Model and Decipher Inter-Organ Communication, *Trends Biotechnol.*, 2021, S0167779920303097.
9 C. M. Leung, P. de Haan, K. Ronaldson-Bouchard, G.-A. Kim, J. Ko and H. S. Rho, A guide to the organ-on-a-chip, *Nat. Rev. Methods Primers*, 2022, **2**, 33.
10 L. J. Y. Ong, T. Ching, L. H. Chong, S. Arora, H. Li and M. Hashimoto, *et al.*, Self-aligning Tetris-Like (TILE) modular microfluidic platform for mimicking multi-organ interactions, *Lab Chip*, 2019, **19**, 2178–2191.
11 C. Oleaga, C. Bernabini, A. S. T. Smith, B. Srinivasan, M. Jackson and W. McLamb, *et al.*, Multi-Organ toxicity demonstration in a functional human *in vitro* system composed of four organs, *Sci. Rep.*, 2016, **6**, 20030.

Open Access Article. Published on 02 December 2024. Downloaded on 5/13/2026 2:24:47 PM. This article is licensed under a Creative Commons Attribution-NonCommercial 3.0 Unported Licence.

12 J. H. Sung, Y. I. Wang, N. Narasimhan Sriram, M. Jackson, C. Long and J. J. Hickman, *et al.*, Recent Advances in Body-on-a-Chip Systems, *Anal. Chem.*, 2019, **91**, 330–351.
13 A. Rezaei Kolahchi, N. Khadem Mohtaram, H. Pezeshgi Modarres, M. Mohammadi, A. Geraili and P. Jafari, *et al.*, Microfluidic-Based Multi-Organ Platforms for Drug Discovery, *Micromachines*, 2016, **7**, 162.
14 C. D. Edington, W. L. K. Chen, E. Geishecker, T. Kassis, L. R. Soenksen and B. M. Bhushan, *et al.*, Interconnected Microphysiological Systems for Quantitative Biology and Pharmacology Studies, *Sci. Rep.*, 2018, **8**, 4530.
15 I. Wagner, E.-M. Materne, S. Brincker, U. Süßbier, C. Frädrich and M. Busek, *et al.*, A dynamic multi-organ-chip for long-term cultivation and substance testing proven by 3D human liver and skin tissue co-culture, *Lab Chip*, 2013, **13**, 3538.
16 A. Chramiec, D. Teles, K. Yeager, A. Marturano-Kruik, J. Pak and T. Chen, *et al.*, Integrated human organ-on-a-chip model for predictive studies of anti-tumor drug efficacy and cardiac safety, *Lab Chip*, 2020, **20**, 4357–4372.
17 T. Satoh, S. Sugiura, K. Shin, R. Onuki-Nagasaki, S. Ishida and K. Kikuchi, *et al.*, A multi-throughput multi-organ-on-a-chip system on a plate formatted pneumatic pressure-driven medium circulation platform, *Lab Chip*, 2018, **18**, 115–125.
18 S. Xiao, J. R. Coppeta, H. B. Rogers, B. C. Isenberg, J. Zhu and S. A. Olalekan, *et al.*, A microfluidic culture model of the human reproductive tract and 28-day menstrual cycle, *Nature Communications*, 2017, **8**, 14584.
19 K. Ronaldson-Bouchard, D. Teles, K. Yeager, D. N. Tavakol, Y. Zhao and A. Chramiec, *et al.*, A multi-organ chip with matured tissue niches linked by vascular flow, *Nat. Biomed. Eng.*, 2022, **6**, 351–371.
20 A. Skardal, S. V. Murphy, M. Devarasetty, I. Mead, H.-W. Kang and Y.-J. Seol, *et al.*, Multi-tissue interactions in an integrated three-tissue organ-on-a-chip platform, *Sci. Rep.*, 2017, **7**, 8837.
21 H. Campo, D. Zha, P. Pattarawat, J. Colina, D. Zhang and A. Murphy, *et al.*, A new tissue-agnostic microfluidic device to model physiology and disease, the lattice platform, *Lab Chip*, 2023, **23**, 4821–4833.
22 K. Shinha, W. Nihei, H. Nakamura, T. Goto, T. Kawanishi and N. Ishida, *et al.*, A Kinetic Pump Integrated Microfluidic Plate (KIM-Plate) with High Usability for Cell Culture-Based Multiorgan Microphysiological Systems, *Micromachines*, 2021, **12**, 1007.
23 V. V. T. Nguyen, S. Ye, V. Gkouzioti, M. E. Van Wolferen, F. Y. Yengej and D. Melkert, *et al.*, A human kidney and liver organoid-based multi-organ-on-a-chip model to study the therapeutic effects and biodistribution of mesenchymal stromal cell-derived extracellular vesicles, *J. Extracell. Vesicles*, 2022, **11**, 12280.
24 Y. Baert, I. Ruetschle, W. Cools, A. Oehme, A. Lorenz and U. Marx, *et al.*, A multi-organ-chip co-culture of liver and testis equivalents, a first step toward a systemic male reprotoxicity model, *Hum. Reprod.*, 2020, **35**, 1029–1044.
25 W. Zhang, Y. S. Zhang, S. M. Bakht, J. Aleman, S. R. Shin and K. Yue, *et al.*, Elastomeric free-form blood vessels for interconnecting organs on chip systems, *Lab Chip*, 2016, **16**, 1579–1586.
26 S. A. P. Rajan, J. Sherfey, S. Ohri, L. Nichols, J. T. Smith and P. Parekh, *et al.*, A Novel Milli-fluidic Liver Tissue Chip with Continuous Recirculation for Predictive Pharmacokinetics Applications, *AAPS J.*, 2023, **25**, 102.
27 S. Shim, M. C. Belanger, A. R. Harris, J. M. Munson and R. R. Pompano, Two-way communication between *ex vivo* tissues on a microfluidic chip, application to tumor–lymph node interaction, *Lab Chip*, 2019, **19**, 1013–1026.
28 D. Bovard, A. Sandoz, K. Luettich, S. Frentzel, A. Iskandar and D. Marescotti, *et al.*, A lung/liver-on-a-chip platform for acute and chronic toxicity studies, *Lab Chip*, 2018, **18**, 3814–3829.
29 H. Kimura, T. Ikeda, H. Nakayama, Y. Sakai and T. Fujii, An On-Chip Small Intestine–Liver Model for Pharmacokinetic Studies, *J. Lab. Autom.*, 2015, **20**, 265–273.
30 E.-M. Materne, A. P. Ramme, A. P. Terrasso, M. Serra, P. M. Alves and C. Brito, *et al.*, A multi-organ chip co-culture of neurospheres and liver equivalents for long-term substance testing, *J. Biotechnol.*, 2015, **205**, 36–46.
31 J. Theobald, M. A. Abu El Maaty, N. Kusterer, B. Wetterauer, M. Wink and X. Cheng, *et al.*, *In vitro* metabolic activation of vitamin D3 by using a multi-compartment microfluidic liver-kidney organ on chip platform, *Sci. Rep.*, 2019, **9**, 4616.
32 A. Herland, B. M. Maoz, D. Das, M. R. Somayaji, R. Prantil-Baun and R. Novak, *et al.*, Quantitative prediction of human pharmacokinetic responses to drugs *via* fluidically coupled vascularized organ chips, *Nat. Biomed. Eng.*, 2020, **4**, 421–436.
33 R. Novak, M. Ingram, S. Marquez, D. Das, A. Delahanty and A. Herland, *et al.*, Robotic fluidic coupling and interrogation of multiple vascularized organ chips, *Nat. Biomed. Eng.*, 2020, **4**, 407–420.
34 P. Loskill, S. G. Marcus, A. Mathur, W. M. Reese and K. E. Healy, μOrgano: A Lego®-Like Plug & Play System for Modular Multi-Organ-Chips, *PLoS One*, 2015, **10**, e0139587.
35 I. Maschmeyer, A. K. Lorenz, K. Schimek, T. Hasenberg, A. P. Ramme and J. Hübner, *et al.*, A four-organ-chip for interconnected long-term co-culture of human intestine, liver, skin and kidney equivalents, *Lab Chip*, 2015, **15**, 2688–2699.
36 M. Trapecar, C. Communal, J. Velazquez, C. A. Maass, Y.-J. Huang and K. Schneider, *et al.*, Gut-Liver Physiomimetics Reveal Paradoxical Modulation of IBD-Related Inflammation by Short-Chain Fatty Acids, *Cell Syst.*, 2020, **10**, 223–239.e9.
37 M. Trapecar, E. Wogram, D. Svoboda, C. Communal, A. Omer and T. Lungjangwa, *et al.*, Human physiomimetic model integrating microphysiological systems of the gut, liver, and brain for studies of neurodegenerative diseases, *Sci. Adv.*, 2021, **7**, eabd1707.
38 Z. Xu, E. Li, Z. Guo, R. Yu, H. Hao and Y. Xu, *et al.*, Design and Construction of a Multi-Organ Microfluidic Chip

 This journal is © The Royal Society of Chemistry 2025

Open Access Article. Published on 02 December 2024. Downloaded on 5/13/2026 2:24:47 PM. This article is licensed under a Creative Commons Attribution-NonCommercial 3.0 Unported Licence.

Mimicking the *in vivo* Microenvironment of Lung Cancer Metastasis, *ACS Appl. Mater. Interfaces*, 2016, **8**, 25840–25847.

39 A. P. Iakovlev, A. S. Erofeev and P. V. Gorelkin, Novel Pumping Methods for Microfluidic Devices, A Comprehensive Review, *Biosensors*, 2022, **12**, 956.

40 D. R. Miller, D. K. Schaffer, M. D. Neely, E. S. McClain, A. R. Travis and F. E. Block, *et al.*, A bistable, multiport valve enables microformulators creating microclinical analyzers that reveal aberrant glutamate metabolism in astrocytes derived from a tuberous sclerosis patient, *Sens. Actuators, B*, 2021, **341**, 129972.

41 B. Jo, Y. Morimoto and S. Takeuchi, 3D-Printed Centrifugal Pump Driven by Magnetic Force in Applications for Microfluidics in Biological Analysis, *Adv. Healthcare Mater.*, 2022, **11**(24), DOI: **10.1002/adhm.202200593**.

42 A.-G. Niculescu, C. Chircov, A. C. Bîrcă and A. M. Grumezescu, Fabrication and Applications of Microfluidic Devices: A Review, *IJMS*, 2021, **22**, 2011.

43 L. A. Milton, M. S. Viglione, L. J. Y. Ong, G. P. Nordin and Y.-C. Toh, Vat photopolymerization 3D printed microfluidic devices for organ-on-a-chip applications, *Lab Chip*, 2023, **23**, 3537–3560.

44 R. G. Mannino, A. N. Santiago-Miranda, P. Pradhan, Y. Qiu, J. C. Mejias and S. S. Neelapu, *et al.*, 3D microvascular model recapitulates the diffuse large B-cell lymphoma tumor microenvironment *in vitro*, *Lab Chip*, 2017, **17**, 407–414.

45 L. Cucullo, N. Marchi, M. Hossain and D. Janigro, A Dynamic *in vitro* BBB Model for the Study of Immune Cell Trafficking into the Central Nervous System, *J. Cereb. Blood Flow Metab.*, 2011, **31**, 767–777.

46 N. Gjorevski, B. Avignon, R. Gérard, L. Cabon, A. B. Roth and M. Bscheider, *et al.*, Neutrophilic infiltration in organ-on-a-chip model of tissue inflammation, *Lab Chip*, 2020, **20**, 3365–3374.

47 Q. Ramadan and F. C. W. Ting, *In vitro* micro-physiological immune-competent model of the human skin, *Lab Chip*, 2016, **16**, 1899–1908.

48 T. Ozulumba, A. N. Montalbine, J. E. Ortiz-Cárdenas and R. R. Pompano, New tools for immunologists: models of lymph node function from cells to tissues, *Front. Immunol.*, 2023, **14**, 1183286.

49 Y. Shou, S. C. Johnson, Y. J. Quek, X. Li and A. Tay, Integrative lymph node-mimicking models created with biomaterials and computational tools to study the immune system, *Mater. Today Bio*, 2022, **14**, 100269.

50 C. L. Willard-Mack, Normal Structure, Function, and Histology of Lymph Nodes, *Toxicol. Pathol.*, 2006, **34**, 409–424.

51 G. A. Roth, V. C. T. M. Picece, B. S. Ou, W. Luo, B. Pulendran and E. A. Appel, Designing spatial and temporal control of vaccine responses, *Nat. Rev. Mater.*, 2021, **7**, 174–195.

52 A. E. Ross and R. R. Pompano, Diffusion of cytokines in live lymph node tissue using microfluidic integrated optical imaging, *Anal. Chim. Acta*, 2018, **1000**, 205–213.

53 A. E. Ross, M. C. Belanger, J. F. Woodroof and R. R. Pompano, Spatially resolved microfluidic stimulation of lymphoid tissue *ex vivo*, *Analyst*, 2017, **142**, 649–659.

54 T. Kraus, A. Lubitz, U. Schließer, C. Giese, J. Reuschel and R. Brecht, *et al.*, Evaluation of a 3D Human Artificial Lymph Node as Test Model for the Assessment of Immunogenicity of Protein Aggregates, *J. Pharm. Sci.*, 2019, **108**, 2358–2366.

55 A. Shanti, B. Samara, A. Abdullah, N. Hallfors, D. Accoto and J. Sapudom, *et al.*, Multi-Compartment 3D-Cultured Organ-on-a-Chip: Towards a Biomimetic Lymph Node for Drug Development, *Pharmaceutics*, 2020, **12**, 464.

56 L. E. Wagar, A. Salahudeen, C. M. Constantz, B. S. Wendel, M. M. Lyons and V. Mallajosyula, *et al.*, Modeling human adaptive immune responses with tonsil organoids, *Nat. Med.*, 2021, **27**, 125–135.

57 G. Goyal, P. Prabhala, G. Mahajan, B. Bausk, T. Gilboa and L. Xie, *et al.*, Ectopic Lymphoid Follicle Formation and Human Seasonal Influenza Vaccination Responses Recapitulated in an Organ-on-a-Chip, *Adv. Sci.*, 2022, **9**, 2103241.

58 S. B. Shah, C. R. Carlson, K. Lai, Z. Zhong, G. Marsico and K. M. Lee, *et al.*, Combinatorial treatment rescues tumour-microenvironment-mediated attenuation of MALT1 inhibitors in B-cell lymphomas, *Nat. Mater.*, 2023, **22**, 511–523.

59 P. Moura Rosa, N. Gopalakrishnan, H. Ibrahim, M. Haug and Ø. Halaas, The intercell dynamics of T cells and dendritic cells in a lymph node-on-a-chip flow device, *Lab Chip*, 2016, **16**, 3728–3740.

60 R. Jeger-Madiot, D. Planas, I. Staropoli, H. Debarnot, J. Kervevan and H. Mary, *et al.*, Modeling memory B cell responses in a lymphoid organ-chip to evaluate mRNA vaccine boosting, *J. Exp. Med.*, 2024, **221**, e20240289.

61 C. Mazzaglia, H. Munir, I. M. Lei, M. Gerigk, Y. Y. S. Huang and J. D. Shields, Modeling Structural Elements and Functional Responses to Lymphatic-Delivered Cues in a Murine Lymph Node on a Chip, *Adv. Healthcare Mater.*, 2024, **13**, 2303720.

62 R. G. Higbee, A. M. Byers, V. Dhir, D. Drake, H. G. Fahlenkamp and J. Gangur, *et al.*, An Immunologic Model for Rapid Vaccine Assessment — A Clinical Trial in a Test Tube, *ATLA, Altern. Lab. Anim.*, 2009, **37**, 19–27.

63 L. M. Delong and A. E. Ross, Open multi-organ communication device for easy interrogation of tissue slices, *Lab Chip*, 2023, **23**, 3034–3049.

64 S. Glushakova, B. Baibakov, L. B. Margolis and J. Zimmerberg, Infection of human tonsil histocultures: A model for HIV pathogenesis, *Nat. Med.*, 1995, **1**, 1320–1322.

65 A. Introini, C. Vanpouille, W. Fitzgerald, K. Broliden and L. Margolis, *Ex Vivo* Infection of Human Lymphoid Tissue and Female Genital Mucosa with Human Immunodeficiency Virus 1 and Histoculture, *J. Visualized Exp.*, 2018, 57013.

66 D. Majorova, E. Atkins, H. Martineau, I. Vokral, D. Oosterhuis and P. Olinga, *et al.*, Use of Precision-Cut Tissue

Open Access Article. Published on 02 December 2024. Downloaded on 5/13/2026 2:24:47 PM. This article is licensed under a Creative Commons Attribution-NonCommercial 3.0 Unported Licence.

Slices as a Translational Model to Study Host-Pathogen Interaction, *Front. Vet. Sci.*, 2021, **8**, 686088.
67 O. Gonzales-Viera, K. D. Woolard and M. K. Keel, Lung and lymph node explants to study the interaction between host cells and canine distemper virus, *Res. Vet. Sci.*, 2023, **154**, 44–51.
68 M. C. Belanger, A. G. Ball, M. A. Catterton, A. W. L. Kinman, P. Anbaei and B. D. Groff, *et al.*, Acute Lymph Node Slices Are a Functional Model System to Study Immunity *Ex Vivo*, *ACS Pharmacol. Transl. Sci.*, 2021, **4**, 128–142.
69 A. Rountree, A. Karkamkar, G. Khalil, A. Folch, D. L. Cook and I. R. Sweet, BaroFuse, a novel pressure-driven, adjustable-throughput perfusion system for tissue maintenance and assessment, *Heliyon*, 2016, **2**, e00210.
70 S. Schneider, M. Bubeck, J. Rogal, H. J. Weener, C. Rojas and M. Weiss, *et al.*, Peristaltic on-chip pump for tunable media circulation and whole blood perfusion in PDMS-free organ-on-chip and Organ-Disc systems, *Lab Chip*, 2021, **21**, 3963–3978.
71 M. B. Esch, H. Ueno, D. R. Applegate and M. L. Shuler, Modular, pumpless body-on-a-chip platform for the co-culture of GI tract epithelium and 3D primary liver tissue, *Lab Chip*, 2016, **16**, 2719–2729.
72 G. M. Walker and D. J. Beebe, A passive pumping method for microfluidic devices, *Lab Chip*, 2002, **2**, 131.
73 L. Chen, Y. Yang, H. Ueno and M. B. Esch, Body-in-a-Cube: a microphysiological system for multi-tissue co-culture with near-physiological amounts of blood surrogate, *Microphysiol. Syst.*, 2020, **4**, 1.
74 P. Fathi, G. Holland, D. Pan and M. B. Esch, Lymphatic Vessel on a Chip with Capability for Exposure to Cyclic Fluidic Flow, *ACS Appl. Bio Mater.*, 2020, **3**, 6697–6707.
75 S. R. Cook, H. B. Musgrove, A. L. Throckmorton and R. R. Pompano, Microscale impeller pump for recirculating flow in organs-on-chip and microreactors, *Lab Chip*, 2022, **22**, 605–620.
76 H. Kimura, T. Yamamoto, H. Sakai, Y. Sakai and T. Fujii, An integrated microfluidic system for long-term perfusion culture and on-line monitoring of intestinal tissue models, *Lab Chip*, 2008, **8**, 741.
77 A. P. Kuo, N. Bhattacharjee, Y. Lee, K. Castro, Y. T. Kim and A. Folch, High-Precision Stereolithography of Biomicrofluidic Devices, *Adv. Mater. Technol.*, 2019, **4**, 1800395.
78 H. B. Musgrove, S. R. Cook and R. R. Pompano, Parylene-C Coating Protects Resin-3D-Printed Devices from Material Erosion and Prevents Cytotoxicity toward Primary Cells, *ACS Appl. Bio Mater.*, 2023, **6**, 3079–3083.
79 C. A. Schneider, W. S. Rasband and K. W. Eliceiri, NIH Image to ImageJ: 25 years of image analysis, *Nat. Methods*, 2012, **9**, 671–675.
80 B. D. Groff, A. W. L. Kinman, J. F. Woodroof and R. R. Pompano, Immunofluorescence staining of live lymph node tissue slices, *J. Immunol. Methods*, 2019, **464**, 119–125.
81 P. Ewels, M. Magnusson, S. Lundin and M. Käller, MultiQC: summarize analysis results for multiple tools and samples in a single report, *Bioinformatics*, 2016, **32**, 3047–3048.
82 M. Martin, Cutadapt Removes Adapter Sequences From High-Throughput Sequencing Reads, *EMBnet J.*, 2011, 10–12.
83 A. Dobin, C. A. Davis, F. Schlesinger, J. Drenkow, C. Zaleski and S. Jha, *et al.*, STAR: ultrafast universal RNA-seq aligner, *Bioinformatics*, 2013, **29**, 15–21.
84 M. I. Love, W. Huber and S. Anders, Moderated estimation of fold change and dispersion for RNA-seq data with DESeq2, *Genome Biol.*, 2014, **15**, 550.
85 A. Liberzon, A. Subramanian, R. Pinchback, H. Thorvaldsdóttir, P. Tamayo and J. P. Mesirov, Molecular signatures database (MSigDB) 3.0, *Bioinformatics*, 2011, **27**, 1739–1740.
86 A. Liberzon, C. Birger, H. Thorvaldsdóttir, M. Ghandi, J. P. Mesirov and P. Tamayo, The Molecular Signatures Database Hallmark Gene Set Collection, *Cell Syst.*, 2015, **1**, 417–425.
87 A. Liberzon, A Description of the Molecular Signatures Database (MSigDB) Web Site. In: *Stem Cell Transcriptional Networks*, 2014, pp. 153–160.
88 H. B. Musgrove, M. A. Catterton and R. R. Pompano, Applied tutorial for the design and fabrication of biomicrofluidic devices by resin 3D printing, *Anal. Chim. Acta*, 2022, **1209**, 339842.
89 C. Warr, J. C. Valdoz, B. P. Bickham, C. J. Knight, N. A. Franks and N. Chartrand, *et al.*, Biocompatible PEGDA Resin for 3D Printing, *ACS Appl. Bio Mater.*, 2020, **3**, 2239–2244.
90 H. Gong, M. Beauchamp, S. Perry, A. T. Woolley and G. P. Nordin, Optical approach to resin formulation for 3D printed microfluidics, *RSC Adv.*, 2015, **5**, 106621–106632.
91 H. Gong, B. P. Bickham, A. T. Woolley and G. P. Nordin, Custom 3D printer and resin for 18 μm × 20 μm microfluidic flow channels, *Lab Chip*, 2017, **17**, 2899–2909.
92 V. Karamzadeh, M. L. Shen, H. Shafique, F. Lussier and D. Juncker, Nanoporous, Gas Permeable PEGDA Ink for 3D Printing Organ-on-a-Chip Devices, *Adv. Funct. Mater.*, 2024, **34**, 2315035.
93 L. F. Horowitz, A. D. Rodriguez, T. Ray and A. Folch, Microfluidics for interrogating live intact tissues, *Microsyst. Nanoeng.*, 2020, **6**, 69.
94 L. F. Horowitz, A. D. Rodriguez, A. Au-Yeung, K. W. Bishop, L. A. Barner and G. Mishra, *et al.*, Microdissected "cuboids" for microfluidic drug testing of intact tissues, *Lab Chip*, 2021, **21**, 122–142.
95 Y. Huang, J. C. Williams and S. M. Johnson, Brain slice on a chip: opportunities and challenges of applying microfluidic technology to intact tissues, *Lab Chip*, 2012, **12**, 2103.
96 A. D. Rodriguez, L. F. Horowitz, K. Castro, H. Kenerson, N. Bhattacharjee and G. Gandhe, *et al.*, A microfluidic platform for functional testing of cancer drugs on intact tumor slices, *Lab Chip*, 2020, **20**, 1658–1675.
97 M. Astolfi, B. Péant, M. A. Lateef, N. Rousset, J. Kendall-Dupont and E. Carmona, *et al.*, Micro-dissected tumor

 This journal is © The Royal Society of Chemistry 2025

Open Access Article. Published on 02 December 2024. Downloaded on 5/13/2026 2:24:47 PM. This article is licensed under a Creative Commons Attribution-NonCommercial 3.0 Unported Licence.

tissues on chip: an *ex vivo* method for drug testing and personalized therapy, *Lab Chip*, 2016, **16**, 312–325.

98 S. Sivashankar, S. V. Puttaswamy, L.-H. Lin, T.-S. Dai, C.-T. Yeh and C.-H. Liu, Culturing of transgenic mice liver tissue slices in three-dimensional microfluidic structures of PEG-DA (poly(ethylene glycol) diacrylate), *Sens. Actuators, B*, 2013, **176**, 1081–1089.

99 K. H. Dodson, F. D. Echevarria, D. Li, R. M. Sappington and J. F. Edd, Retina-on-a-chip: a microfluidic platform for point access signaling studies, *Biomed. Microdevices*, 2015, **17**, 114.

100 G. Mauleon, C. P. Fall and D. T. Eddington, Precise Spatial and Temporal Control of Oxygen within *In Vitro* Brain Slices *via* Microfluidic Gas Channels, *PLoS One*, 2012, **7**, e43309.

101 P. van Midwoud, T. M. Merema, E. Verpoorte and G. M. M. Groothuis, A microfluidic approach for *in vitro* assessment of interorgan interactions in drug metabolism using intestinal and liver slices, *Lab Chip*, 2010, **10**, 2778–2786.

102 A. E. Cherwin, H. N. Templeton, A. T. Ehrlich, B. H. Patlin, C. S. Henry and S. A. Tobet, Microfluidic organotypic device to test intestinal mucosal barrier permeability *ex vivo*, *Lab Chip*, 2023, **23**, 4126–4133.

103 G. K. Sureshkumar and R. Mutharasan, The influence of temperature on a mouse-mouse hybridoma growth and monoclonal antibody production, *Biotechnol. Bioeng.*, 1991, **37**, 292–295.

104 J. Munson and A. Shieh, Interstitial fluid flow in cancer: implications for disease progression and treatment, *CMAR*, 2014, 317.

105 M. A. Swartz and M. E. Fleury, Interstitial Flow and Its Effects in Soft Tissues, *Annu. Rev. Biomed. Eng.*, 2007, **9**, 229–256.

106 M. Jafarnejad, M. C. Woodruff, D. C. Zawieja, M. C. Carroll and J. E. Moore, Modeling Lymph Flow and Fluid Exchange with Blood Vessels in Lymph Nodes, *Lymphatic Res. Biol.*, 2015, **13**, 234–247.

107 L. J. Cooper, J. P. Heppell, G. F. Clough, B. Ganapathisubramani and T. Roose, An Image-Based Model of Fluid Flow Through Lymph Nodes, *Bull. Math. Biol.*, 2016, **78**, 52–71.

108 J. B. Dixon, S. T. Greiner, A. A. Gashev, G. L. Cote, J. E. Moore and D. C. Zawieja, Lymph Flow, Shear Stress, and Lymphocyte Velocity in Rat Mesenteric Prenodal Lymphatics, *Microcirculation*, 2006, **13**, 597–610.

109 K. S. Sakariassen, L. Orning and V. T. Turitto, The impact of blood shear rate on arterial thrombus formation, *Future Sci. OA*, 2015, **1**, fso.15.28.

110 A. R. Hyler, N. C. Baudoin, M. S. Brown, M. A. Stremler, D. Cimini and R. V. Davalos, *et al.*, Fluid shear stress impacts ovarian cancer cell viability, subcellular organization, and promotes genomic instability, *PLoS One*, 2018, **13**, e0194170.

111 J. A. Schwarz, C. I. Contescu and K. Putyera, *Dekker Encyclopedia of Nanoscience and Nanontechnology*, ed. M. Dekker, New York, 2004.

112 B. J. O'Grady, M. D. Geuy, H. Kim, K. M. Balotin, E. R. Allchin and D. C. Florian, *et al.*, Rapid prototyping of cell culture microdevices using parylene-coated 3D prints, *Lab Chip*, 2021, **21**, 4814–4822.

113 S. Gholizadeh, D. M. Lincoln, Z. Allahyari, L. P. Widom, R. N. Carter and T. R. Gaborski, Optimization of Parylene C and Parylene N thin films for use in cellular co-culture and tissue barrier models, *Sci. Rep.*, 2023, **13**, 4262.

114 B. Lee, S. Kim, J. Ko, S.-R. Lee, Y. Kim and S. Park, *et al.*, 3D micromesh-based hybrid bioprinting: multidimensional liquid patterning for 3D microtissue engineering, *NPG Asia Mater.*, 2022, **14**, 6.

115 M. Pitorre, G. Bastiat, E. M. Dit Chatel and J.-P. Benoit, Passive and specific targeting of lymph nodes: the influence of the administration route, *Eur. J. Nanomed.*, 2015, **7**, 121–128.

116 D. Bertheloot, E. Latz and B. S. Franklin, Necroptosis, pyroptosis and apoptosis: an intricate game of cell death, *Cell. Mol. Immunol.*, 2021, **18**, 1106–1121.

117 M. E. Tóth, L. Vígh and M. Sántha, Alcohol stress, membranes, and chaperones, *Cell Stress Chaperones*, 2014, **19**, 299–309.

118 A. G. Ball, M. C. Belanger and R. R. Pompano, Detergent wash improves vaccinated lymph node handling *ex vivo*, *J. Immunol. Methods*, 2021, **489**, 112943.

119 B. D. Groff, A. W. L. Kinman, J. F. Woodroof and R. R. Pompano, Immunofluorescence staining of live lymph node tissue slices, *J. Immunol. Methods*, 2019, **464**, 119–125.

120 I. A. Ramshaw, A. J. Ramsay, G. Karupiah, M. S. Rolph, S. Mahalingam and J. C. Ruby, Cytokines and immunity to viral infections, *Immunol. Rev.*, 1997, **159**, 119–135.

121 S. Mahalingam, K. Clark, K. I. Matthaei and P. S. Foster, Antiviral potential of chemokines, *BioEssays*, 2001, **23**, 428–435.

122 R. Goswami and M. H. Kaplan, A Brief History of IL-9, *J. Immunol.*, 2011, **186**, 3283–3288.

123 K. Ronaldson-Bouchard and G. Vunjak-Novakovic, Organs-on-a-Chip: A Fast Track for Engineered Human Tissues in Drug Development, *Cell Stem Cell*, 2018, **22**, 310–324.

124 J. M. Rutkowski and M. A. Swartz, A driving force for change: interstitial flow as a morphoregulator, *Trends Cell Biol.*, 2007, **17**, 44–50.

125 M. J. O'Melia, A. W. Lund and S. N. Thomas, The Biophysics of Lymphatic Transport: Engineering Tools and Immunological Consequences, *iScience*, 2019, **22**, 28–43.

126 A. A. Tomei, S. Siegert, M. R. Britschgi, S. A. Luther and M. A. Swartz, Fluid Flow Regulates Stromal Cell Organization and CCL21 Expression in a Tissue-Engineered Lymph Node Microenvironment, *J. Immunol.*, 2009, **183**, 4273–4283.

127 E. M. Bouta, R. W. Wood, E. B. Brown, H. Rahimi, C. T. Ritchlin and E. M. Schwarz, *In vivo* quantification of lymph viscosity and pressure in lymphatic vessels and draining lymph nodes of arthritic joints in mice, *J. Physiol.*, 2014, **592**, 1213–1223.

128 E. Nader, S. Skinner, M. Romana, R. Fort, N. Lemonne and N. Guillot, *et al.*, Blood Rheology: Key Parameters, Impact

Open Access Article. Published on 02 December 2024. Downloaded on 5/13/2026 2:24:47 PM.
This article is licensed under a Creative Commons Attribution-NonCommercial 3.0 Unported Licence.

on Blood Flow, Role in Sickle Cell Disease and Effects of Exercise, *Front. Physiol.*, 2019, **10**, 1329.

129 B. Müller, S. Lang, M. Dominietto, M. Rudin, G. Schulz and H. Deyhle, High-resolution tomographic imaging of microvessels, *Development in X-Ray Tomography VI*, 2008, vol. 7078, p. 70780B.

130 H. E. Abaci and M. L. Shuler, Human-on-a-chip design strategies and principles for physiologically based pharmocokinetics/pharmacodynamics modeling, *Integr. Biol.*, 2016, **7**(4), 383–391.

131 C. Moraes, J. M. Labuz, B. M. Leung, M. Inoue, T.-H. Chun and S. Takayama, On being the right size: scaling effects in designing a human-on-a-chip, *Integr. Biol.*, 2013, **5**, 1149.

132 D. Park, J. Lee, J. J. Chung, Y. Jung and S. H. Kim, Integrating Organs-on-Chips: Multiplexing, Scaling, Vascularization, and Innervation, *Trends Biotechnol.*, 2020, **38**, 99–112.

133 C. Stokes, M. Cirit and D. Lauffenburger, Physiome-on-a-Chip: The Challenge of "Scaling" in Design, Operation, and Translation of Microphysiological Systems, *CPT:Pharmacometrics Syst. Pharmacol.*, 2015, **4**, 559–562.

134 J. P. Wikswo, E. L. Curtis, Z. E. Eagleton, B. C. Evans, A. Kole and L. H. Hofmeister, *et al.*, Scaling and systems biology for integrating multiple organs-on-a-chip, *Lab Chip*, 2013, **13**, 3496.

135 C. Fox, H. Sarkisyan, R. Stevens, F. Arabia, W. Fischer and J. Rossano, *et al.*, New versatile dual-support pediatric heart pump, *Artif. Organs*, 2019, **43**, 1055–1064.

136 M. Hirschhorn, E. Bisirri, R. Stevens and A. L. Throckmorton, Fluid-structure interaction analysis of a collapsible axial flow blood pump impeller and protective cage for Fontan patients, *Artif. Organs*, 2020, **44**, 337–347.

This journal is © The Royal Society of Chemistry 2025